Active enhancers strengthen TAD insulation by bRNA mediated CTCF enrichment at the TAD boundaries

Zubairul Islam[1,2*], Bharath Saravanan[1,2*], Kaivalya Walavalkar[1], Umer Farooq [1,3], Anurag Kumar Singh[1], Jitendra Thakur [4], Awadhesh Pandit[1], Radhakrishnan Sabarinathan[1], Steven Henikoff [5], Dimple Notani[1#]

1. Genetics and Development, National Centre for Biological Sciences, Tata Institute for Fundamental Research, Bangalore, Karnataka, 560065. India

2. Sastra Deemed University, Thanjavur, Tamil Nadu, 613401. India

3. The University of Trans-Disciplinary Health Sciences and Technology, IVRI road, Bangalore, Karnataka, 560064. India

4. Department of Biology, Emory University, Atlanta, Georgia, 30322. USA

5. Basic Sciences Division, Fred Hutchinson Cancer Research Centre, 1100 N. Fairview Ave, Seattle, WA, 98109, USA

* Equal contributions

Corresponding author: dnotani@ncbs.res.in

Abstract:

The genome is partitioned into Topologically Associating Domains (TADs). About half of the boundaries of these TADs exhibit transcriptional activity and are correlated with better TAD insulation. However, the role of these transcripts *per se* in TAD insulation, enhancer:promoter interactions and transcription remain unknown. Here we investigate the functional roles of these bRNAs (boundary-RNA) in boundary insulation and consequent effects on enhancer-promoter interactions and TAD transcription genome-wide and on disease relevant INK4a/ARF TAD. Using series of CTCF sites deletion and bRNA knockdown approaches at this TAD boundary, we show a direct association of CTCF with bidirectional bRNAs where the loss of bRNA triggers the concomitant loss of: CTCF clustering at TAD boundary, its insulation, enhancer:promoter interactions and gene transcription within the targeted TAD. In search of what regulates bRNA expression itself, we used another series of enhancer deletions and CRISPRi on promoters within INK4a/ARF TAD and observed that indeed, enhancers interact with boundaries and positively regulate the bRNA transcription at TAD boundaries. In return, the bRNAs recruit/stabilize the CTCF even on weaker motifs within these boundaries and supports CTCF binding in clusters, therefore enhancing TAD insulation which favors the intra-TAD enhancer:promoter interactions and robust gene transcription. Functionally, eRNAs within the boundaries are repurposed as more stable bRNAs and their knockdown exactly mimics the boundary loss. Furthermore, transcribing boundaries exhibit high TAD transcription in TCGA tumor datasets. Together, these results show that active enhancers directly mediate better insulation of TADs by activating the transcription at TAD boundaries. These transcripts trigger CTCF clustering at the boundary resulting in better insulation which favours robust intra-TAD enhancer:promoter interactions to activate the gene transcription.

Introduction:

Genomes are organized into functional and physical units known as TADs (Topologically associating domains) (Dixon et al., 2012). Highly self-interacting domains are identified as contact domains and the domains that exhibit corner dots (at the apex of loop) are known as loop domains. Most TADs exist as contact domains and is used as an umbrella term for TADs while some TADs are identified as both loop domains and contact domains (Beagan and Phillips-Cremins, 2020). Loop and contact domains are both proposed to be formed by loop extrusion (Dekker and Mirny, 2016; Dixon et al., 2012; Fudenberg et al., 2016; Nuebler et al., 2018; Rao et al., 2014; Szabo et al., 2020), and are dependent on CTCF and cohesin (Nora et al., 2017; Rao et al., 2017; Schwarzer et al., 2017; Wutz et al., 2017). Length of the extruded loop is determined by the presence and orientation of CTCF bound regions which contains interactions within the loop (Rao et al., 2014). Thus, by not allowing the enhancers and promoters to interact outside of the loops, CTCF strength and number of binding sites at boundaries provides greater insulation of the TAD (Krivega and Dean, 2017; Nora et al., 2017; Rowley et al., 2017). However, CTCF consensus motif or their orientation predict TADs boundaries less accurately suggesting, additional factors must influence the CTCF binding and therefore TAD formation/insulation.

The perturbations in CTCF sites at the boundaries have shown none to severe effects on gene transcription in the same and neighbouring TADs (Despang et al., 2019; Flavahan et al., 2016; Hanssen et al., 2017; Kloetgen et al., 2020; Narendra et al., 2015; Sima et al., 2019; Williamson et al., 2019; Yang et al., 2019). Within these observations, perturbation of all of the CTCF sites within the boundary region or acute depletion of CTCF is essential to display effects on transcription (Khoury et al., 2020; Williamson et al., 2019) suggesting, a redundancy among the multiple CTCF sites at the TAD boundary. However, how multiple CTCF sites within the boundary coordinate to achieve better insulation requires interrogations.

Further, transcription at the boundaries is correlated with better insulation and CTCF occupancy (Bonev et al., 2017; Hsieh et al., 2020; Khoury et al., 2020) explaining, why transcription inhibition or RNaseA treatments affect genome architecture (Barutcu et al., 2019, Thakur et al., 2019). Furthermore, CTCF dimerization, important for loop extrusion, is RNA dependent and RNA

binding of CTCF is required for genome organization (Hansen et al., 2019; Saldaña-Meyer et al., 2019), but how CTCF:RNA interactions maintain the TAD organization is not clear. Further, which RNAs and their sites of transcription that are involved in such organizer functions is not known.

Furthermore, if active TADs utilise these RNA mediated mechanisms to strengthen the TAD boundaries remains completely unknown. For example, if these observed effects on chromatin architecture are the result of transcription or transcripts from, intra TAD regions or from the boundaries remains an interesting aspect of this conundrum. Further, if RNA transcription/transcripts at the TAD boundaries influence enhancer:promoter interactions and gene transcription remains unknown.

Interestingly, the TADs with super enhancers exhibit strong boundaries (Gong et al., 2018; D. Zhang et al., 2020). Enhancers and boundaries are also known to interact with each other in some instances (NandyMazumdar et al., 2020). However, if these enhancers play an active role in boundary insulation or if there is a regulatory relationship between these two type of elements remains to be tested.

Here we show that boundaries of about half of the TADs (with and without corner dots) exhibit ongoing transcriptional activity either from a gene-body that is overlapping with boundary region or from non-genic region that transcribes *de novo* non-coding RNAs within boundary. The transcribing boundaries (non-genic and genic) show more CTCF enrichment and number of CTCF peaks resulting in better TAD insulation (with and without corner dots). Further, we observed genome-wide high corroboration between higher transcription at boundaries with the higher transcriptional state of the genes within the TAD. Furthermore, the non-coding RNAs within non-genic boundaries are transcribed from enhancers like regions however; these RNAs are more stable, have relatively higher presence of 5' splicing sites and exhibit less abundance of transcription termination signal (TTS) than eRNAs. Similarly, the genic transcripts from the boundaries also exhibit more stability as compared to other mRNAs. Due to these distinct features of RNA (coding, long non-coding and eRNAs) transcribing from boundaries, we name them bRNAs (Boundary-RNAs). One such non-genic boundary shows *de novo* bRNA transcribing from

two CTCF sites at the INK4a/ARF locus TAD. These bRNAs and CTCF physically interact with one another and knockdown of these sense and anti-sense bRNAs triggers the loss of CTCF at the boundary and also results in down regulation of genes within INK4a/ARF TAD which is similar to the deletion of these two CTCF sites. This TAD also harbours a super enhancer and the deletions of multiple enhancers within SE reveals that indeed active enhancers regulate the *de novo* bRNA transcription by direct physical interactions between these enhancers and boundary elements. Transcriptional activity of promoters, however, has no effect on *de novo* bRNA expression. Both, CTCF sites deletions and bRNA knockdown results in the loss of enhancer:promoter interactions but strengthened interactions of the enhancers with regions outside the TAD. These observations suggest that active enhancers directly assist in TAD insulation by triggering the transcription at the boundaries. The bRNA transcripts then recruit CTCF at the boundary and thus enhancers are enforced to interact more with promoters in the same TAD resulting in robust intra-TAD transcription.

Results:

RNA transcribing boundaries exhibit better insulation

Transcriptional inhibition by either DRB or α-amanitin alters the chromatin architecture (Hsieh et al., 2020, Barutcu et al., 2019). This suggests that the transcriptional activity or the RNA *per se* play a role in genome organization. Further, the active transcription at the TAD boundaries has been speculated to play a role in TAD strength (Giorgetti et al., 2016; D. Zhang et al., 2020; Zhang et al., 2019). Similarly, severe depletion of CTCF, an enriched factor at TAD boundaries also affects the chromatin architecture (Khoury et al., 2020; Nakahashi et al., 2013; Nuebler et al., 2018; Pugacheva et al., 2020). Thus, we asked if there is any association between the transcriptional activity at the TAD boundaries and CTCF occupancy. Towards this, we first interrogated the proportion of genome-wide TAD boundaries that transcribe RNA using GRO-seq (Andersson et al., 2014). In order to identify boundaries, we employed HOMER that uses a high degree of intra-domain interactions to their surrounding regions for TAD calling. As a result, it identifies contact domain TADs, with corner dot (loop domains) and without corner-dot. Both, TADs and loops are proposed to be formed by loop extrusion and are dependent on CTCF and

cohesin (Nora et al., 2017; Rao et al., 2017; Schwarzer et al., 2017; Wutz et al., 2017). We identified 15397 TADs boundaries (5 kb resolution) using HiC from HeLa (Rao et al., 2014). Within these, 8134 TADs boundaries (52.8%) showed presence of nascent transcripts in GRO-seq. Several TAD boundaries have overlapping genes within them. Thus, we tested the extent of these boundaries transcribing RNA as a result of genic transcription overlapping with boundary region. We stratified the TAD boundaries into two categories; the boundaries with presence of transcripts that arise from overlapping genes (gene body) with boundary (5 kb region), and the boundaries where the transcription originates from within the boundaries (5 kb) but without the presence of any gene (*de novo* non-coding transcription) (Fig. 1A-B). 41.56% (6406) out of 15397 had genic transcripts. Whereas, 11.22% (1728) boundaries showed *de novo* non-coding transcription (Fig. 1A, C). These data suggest that a large majority of TAD boundaries show ongoing transcriptional activity. Further, several boundaries exhibit *de novo* transcription originating as non-coding RNA. We label both, genic and non-genic boundaries as RNA transcribing boundaries. Note, most RNA transcribing boundaries (78.75%) are genic and remaining (21.25%) are non-genic boundaries.

TAD boundaries are enriched for CTCF binding and it also plays an important role in loop extrusion. Thus, to test the correlation between strength of CTCF occupancy and presence of transcription, we assessed the levels of CTCF on the genic, non-genic and non-transcribing boundaries. To rule out the biased enrichment of CTCF due to chemical fixation used in standard ChIP protocol, we used Cut & Run data. Total CTCF signal was calculated at these boundaries using CTCF Cut & Run data (Skene and Henikoff, 2017) and we observed that genic and non-genic RNA transcribing boundaries had significantly higher CTCF enrichment as compared to non-transcribing boundaries (Fig. 1D). This correlation in (Fig. 1D) was also evident on all the boundaries segregated based on RNA expression levels (Fig. 1E) (Top 1500 (10%) boundaries out of the 15397, with respect to the GRO-seq signal is classified as high, 1500 non-zero low GRO-seq signal as Low, random 1500 zero GRO-seq signal as None and 1500 random boundaries from 15397 classified as random boundaries). Further, within non-genic transcribing boundaries, we observed that CTCF enrichment was correlated with the levels of RNA transcription (600 boundaries in all categories (10% of all non-genic boundaries)) (Fig. S1A-B). Interestingly, even the non-genic boundaries with lowest transcriptional activity exhibited higher CTCF enrichments as compared to non-transcribing boundaries (Fig. S1A). The same trend of CTCF correlation with

RNA presence on all, genic and non-genic boundaries was noted with CTCF ChIP-seq (with formaldehyde fixed cells (Zhang et al., 2020)) (Fig. S1C-E). Taken together, the transcribing boundaries exhibit higher CTCF binding as compared to non-transcribing and random boundaries in the genome (Fig. 1D-E, S1A-E).

Boundaries insulate TADs by favoring intra-TAD interactions and their strength is measured by insulation scores using HiC data. We asked if the various classes of TAD boundaries that are also transcribing and show high CTCF binding indeed have differential insulation strength. Interestingly, we noted a higher insulation of genic and non-genic transcribing boundaries as compared to non-transcribing boundaries (Fig. 1F). Further, the insulation score was positively corelated with the RNA levels in all transcribing boundaries (Fig. 1G) and non-genic transcribing boundaries (Fig. S1F). Even the TADs with least transcribing non-genic boundaries were better insulated as compared to non-transcribing boundaries (Fig. S1F) (Here, higher insulation score refers to better insulation). To rule out resolution related biases, we extended the 5kb windows of TAD boundary to 20 kb and these observations were found to be replicated even then (Fig. S2). For example, total 69.2% (10658) out of 15397 TADs boundaries were found to be transcribing (Fig. S2A). The CTCF enrichment on All, genic and non-genic boundaries even at 20 kb distance was true as for 5 kb (Fig. S2B-E). Insulation score also followed the same trend (Fig. S2F-H).

Further, to test if the positive correlation between transcribing boundaries and CTCF enrichment is also true on domains called by yet another method, we used HICCUPS (Algorithm of the Juicer Software suite) that identifies loop domains. In total 3525 loop anchors were identified with 5kb boundary region. Out of these, 43.09% (1519) were genic and 19.19% (675) were non-genic boundaries (loop anchors) (Fig. S3A). We found similar positive correlation between transcribing boundaries and extent of transcription on all transcribing boundaries with CTCF enrichment using CTCF cut & run (Fig. S3B-C) and ChIP-seq data (Fig. S3D-E).

These observations of higher CTCF and insulation with extent of transcription at transcribing boundaries were also confirmed in IMR90 (Rao et al., 2014) (Fig. S4A-D) and lymphoblastoid cells K562 (Zirkel et al., 2018) (Fig. S4E-H) suggesting these correlations are relevant in other cancer-type and normal cells. These data reveal the high CTCF occupancy and concurring higher

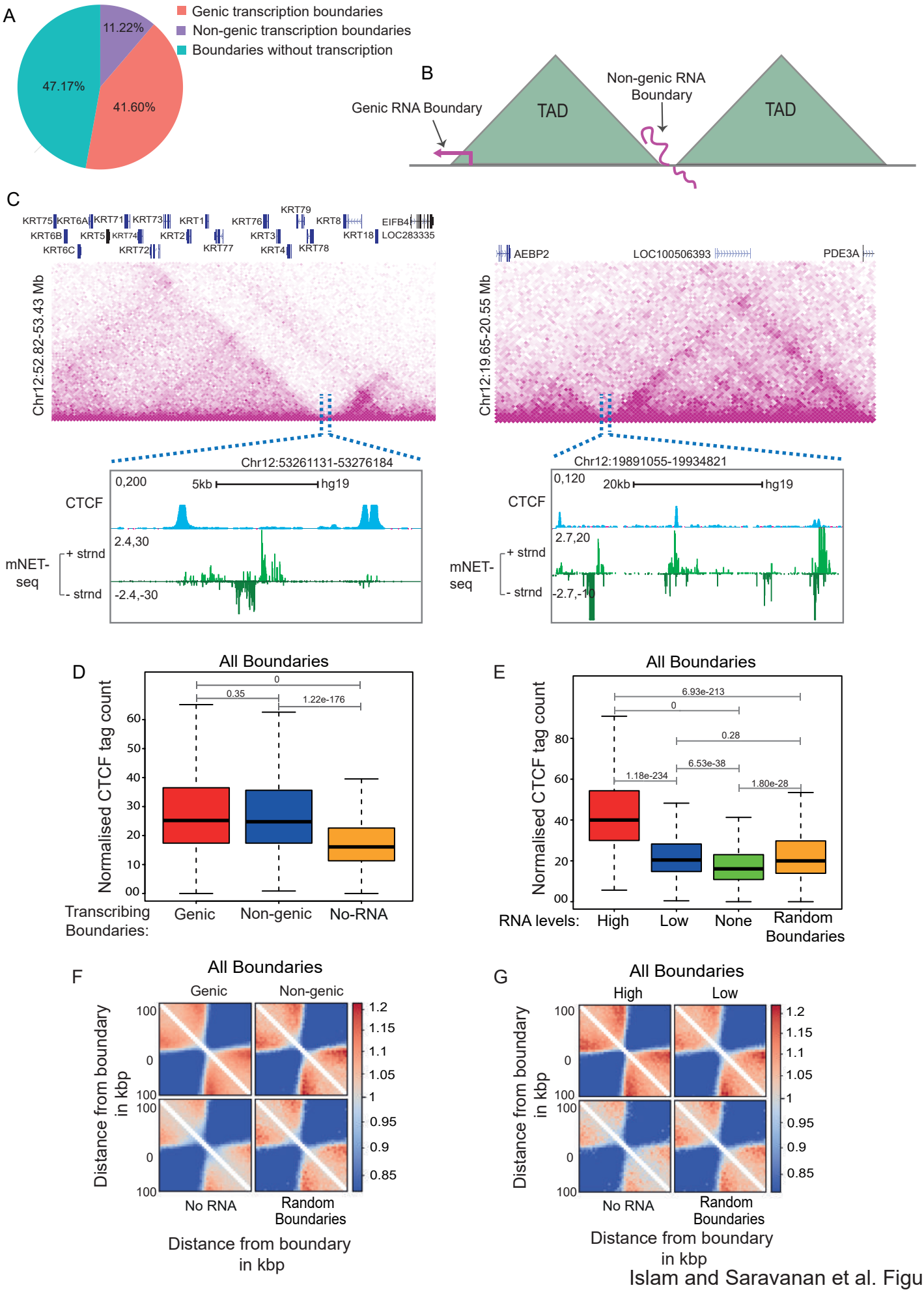

Islam and Saravanan et al. Figure 1

Legends:

Figure 1. RNA transcribing boundaries exhibit better insulation: A. Pie diagram showing the percentage of boundaries that show genic transcription, non-genic de novo transcription and no transcription. **B.** The schematic depicting genic and non-genic transcribing boundaries. **C.** Browser shots displaying TAD structure from HiC data on two regions. The zoomed in box show *de novo* non-genic transcribing boundary region that is overlaid with CTCF and mNET-seq signal. **D.** Box plots showing the CTCF enrichment on genic, non-genic and Non-transcribing boundaries. **E.** Box plots showing the CTCF enrichment on All boundaries exhibiting varying levels of RNAs vs. non-transcribing and random boundaries. **F.** Pile up plot on transcribing genic, non-genic, non-transcribing boundaries and random boundaries. **G.** Pile up plot on high transcribing, low transcribing, non-transcribing and random boundaries. The p-values in boxplots were calculated by Mann Whitney test (Wilcoxon two-sided rank sum test). The boxplots depict the minimum (Q1-1.5*IQR), first quartile, median, third quartile and maximum (Q3+1.5*IQR) without outliers.

insulation score of transcribing boundaries. For the remaining work, we focused on TADs called by HOMER with 5 kb boundary regions.

RNA augments the recruitment of CTCF at the TAD boundary

Since, genic and non-genic transcribing boundaries exhibit high levels of CTCF, we asked if there is a causal relationship between the presence of RNAs (genic RNA or *de novo* non-coding RNA) and CTCF at these sites. Towards this, we first tested the dependency of CTCF on RNA for its chromatin occupancy by chromatin and nucleoplasm fractionations upon RNaseA treatments to HeLa cells. We noticed a significant loss of CTCF in the chromatin fraction upon removal of RNA (Fig. 2A). This data is in concordance with the reported dependence of CTCF on RNA for chromatin binding (Hansen et al., 2019; Saldaña-Meyer et al., 2019, Thakur et al., 2019). To test the relative loss of CTCF on specific sites in the genome upon RNAseA, we performed Cut & Run for CTCF upon RNAseA treatment and interrogated the altered CTCF binding in a genome-wide manner. As expected, integrated CTCF tag counts along the TADs showed highest enrichment of CTCF at the TAD borders (Fig. 2B), and this enrichment at the boundaries was relatively more susceptible to RNAseA treatment as compared to Intra-TAD regions (Fig. 2B). Thus, we asked how RNA might regulate the binding of CTCF at the TAD borders.

We tested if such loss of CTCF at the boundaries is directly mediated via RNA *per se* or the loss of CTCF is an indirect effect of general RNA degradation as seen in RNaseA Cut & Run data (Fig. 2B). Towards this, we performed a series of experiments on a disease relevant *INK4a/ARF* TAD (approx. 500 Kb long) as a model (Fig. 2C). This TAD harbors actively transcribing cell cycle regulatory genes; *CDKN2A*, *CDKN2B* and *MTAP*. The locus also harbors a super-enhancer associated with several GWAS variants (Fig. 2C, high-lighted region) (Farooq et al., 2021; Harismendy et al., 2011). Several enhancers within the super enhancer are active as seen by H3K27ac marks and eRNA expression (Fig. 2C, mNET-seq panel) (Farooq et al., 2021). The 5' boundary of the TAD is within the transcribed gene *MTAP*, whereas the 3' boundary region is non-genic and contains three significant CTCF ChIP-seq peaks (B1, B2 and B3) (Fig. 2C, high-lighted region). Out of these, B1 and B2 CTCF sites exhibited strong nascent transcription as observed by publicly available mNET-seq, GRO-seq and PRO-seq data (Bouvy-Liivrand et al., 2017; Nilson

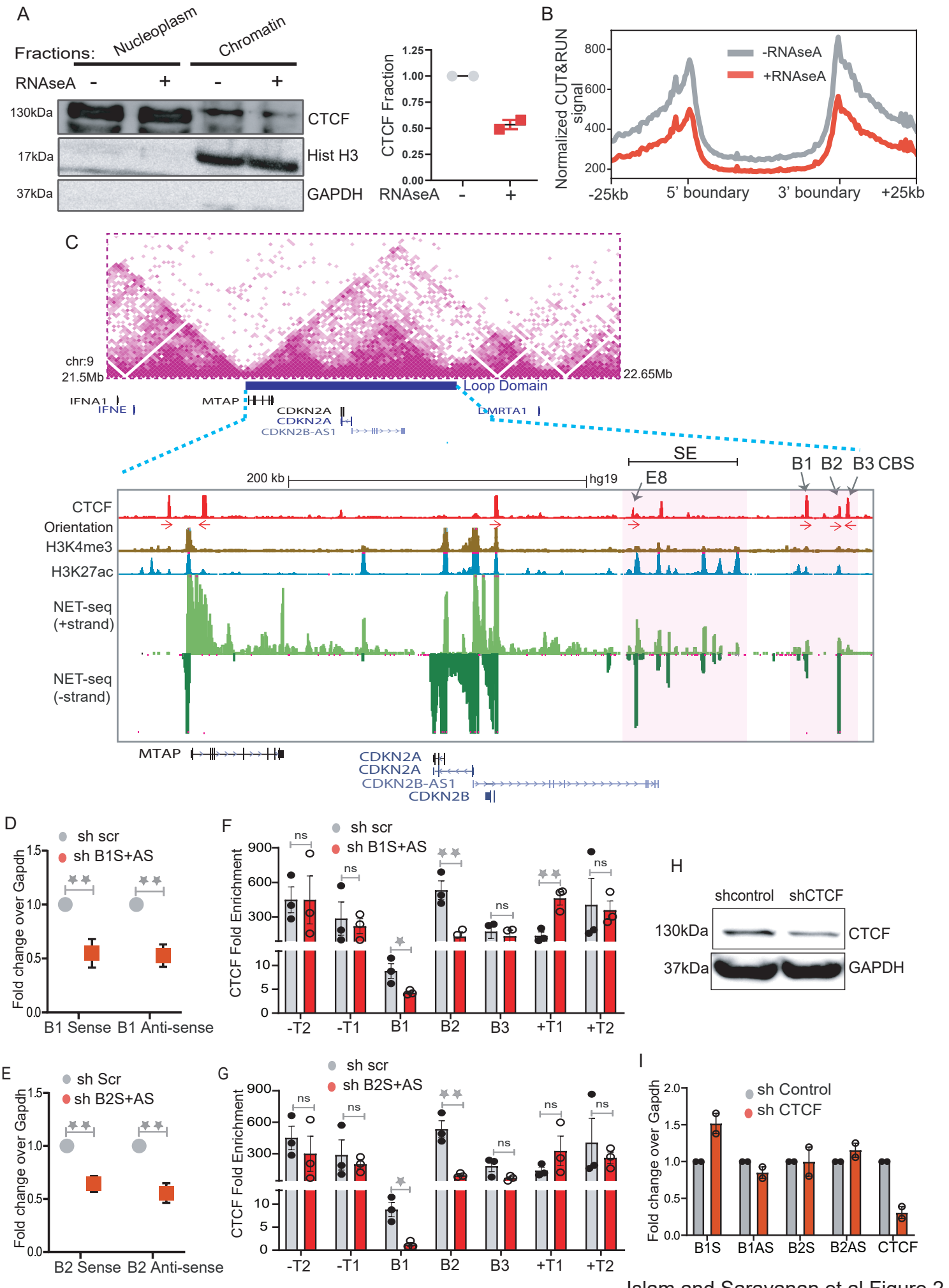

Islam and Saravanan et al Figure 2

Figure 2. RNA augments the recruitment of CTCF at the TAD boundary: A. Immunoblotting with CTCF, Histone H3 and GAPDH on soluble nucleoplasm and chromatin bound fractions of the nucleus treated with or without RNaseA (Left panel). The right panel shows the quantified loss of CTCF from chromatin fractions from two replicates. **B.** Normalised CTCF cut and run signal in control and RNAse A treated conditions plotted at equally scaled TADs of 50kb length each and 25kb flanks**. C.** TAD structure at INK4a/ARF locus on 9p21 region (Rao et al., 2014). The loop domain (Blue bar) is overlaid by the position of CTCF peaks, CTCF motif orientation, H3K4me3, H3K27ac (enhancers), mNET-seq tracks and gene annotations. The highlighted region shows the B1, B2 and B3 CTCF sites on 3' boundary and super enhancer with position of enhancer E8 marked by an arrow. **D.** qRT-PCRs showing the levels of sense and anti-sense non-coding RNA at B1 CTCF site upon B1 RNA knockdown **E.** qRT-PCRs showing the levels of sense and anti-sense RNA at B2 CTCF site upon B2 RNA knockdown. **F.** CTCF ChIP enrichment before and after shRNA mediated knockdown of sense and anti-sense RNA at B1 CTCF sites. The bars show the CTCF on three CTCF sites (B1, B2 and B3) at 3' boundary, on -T1 (5' boundary) of INK4a/ARF TAD, -T2 on adjacent TAD boundary upstream, +T1 (on adjacent TAD boundary downstream) and +T2 the boundary of following TAD downstream. **G.** CTCF ChIP enrichment before and after shRNA mediated knockdown of sense and anti-sense RNA at B2 CTCF sites. The bars show the CTCF on three CTCF sites (B1, B2 and B3) at 3' boundary, on -T1 (5' boundary) of INK4a/ARF TAD, -T2 on adjacent TAD boundary upstream, +T1 (on adjacent TAD boundary downstream) and +T2 the boundary of following TAD downstream. Error bars denote SEM from three biological replicates. *p*-values were calculated by Student's two-tailed unpaired *t*-test in **D, E, F** and **G .** $^{**}p < 0.01, ^{*}p < 0.05, ^{ns}p > 0.05$ **H.** Immunoblot showing the drop in CTCF levels upon CTCF knockdown by the pool of shRNAs. **I.** qRT-PCRs of sense and antisense RNAs from B1 and B2 CTCF sites upon CTCF knockdown. The drop in CTCF levels are shown in the last two bars.

et al., 2017; Schlackow et al., 2017), whereas B3 was weakly transcribed (Fig. 2C, mNET-seq panel and Fig. S5A mNET-seq, GRO-seq and PRO-seq on this TAD) and there was no annotated gene or had reads from the nearest gene suggesting it is a *de novo* non-coding RNA boundary and the CTCF motif within B1 and B2 site is in forward orientation (Fig. 2C, Fig. S5A-B). Since, the removal of RNA by RNaseA treatment showed the loss of CTCF at the boundary regions on this TAD as seen by CTCF Cut & Run upon RNaseA (Fig. S6A), we asked if these non-coding RNAs recruit CTCF at this boundary (B1 and B2 CTCF sites). Towards that end, we depleted non-coding RNAs at B1 and B2 CTCF sites using specific shRNAs against sense and anti-sense RNAs (Fig. 2D and E). We also confirmed the acute knockdown of RNAs at the B1 and B2 CTCF sites in chromatin fraction by qRT-PCRs (Fig. S6B). The CTCF at B1 and B2 sites exhibited loss of CTCF upon such knockdowns of sense and anti-sense RNAs. However, CTCF remained unaffected on B3, the 5' boundary of the same TAD (-T1 site) and on the boundaries of its flanking TADs (-T2 and +T1, +T2) (Fig. 2F-G and Fig. S6C). Interestingly, loss of RNAs at B1 site perturbed the CTCF occupancy at not only B1 but also at B2 site and vice versa (Fig. 2F-G). These results suggest that CTCF on transcribing boundaries is recruited partly via the RNAs and different transcribing CTCF sites within a boundary are potentially interdependent. Notably, shRNA mediated knockdown or over-expression of CTCF had none to marginal effects on non-coding RNA expression (Fig. 2H-I and Fig. S6D), which suggests that CTCF enrichment at TAD boundaries is regulated by RNA but RNA levels are independent of CTCF levels. However, persistent CTCF binding at B1 and B2 sites even after its acute depletion cannot be ruled out and hence, can bias this result.

Non-coding RNAs and CTCF physically interact at 9p21 TAD boundary

Since, CTCF occupancy at B1 and B2 sites was reduced upon RNaseA treatment and RNA knockdowns (Fig. 2), we asked if RNA and CTCF interact as shown on total RNA (Hansen et al., 2019; Saldaña-Meyer et al., 2019) (Fig. 3A). Towards this, we first performed RNA pulldowns on sense and anti-sense RNAs transcribed from B1 and B2 CTCF sites (Fig. S5B). We observed an interaction between these RNAs and CTCF (Fig. 3B). Interestingly, an eRNA from E8 enhancer within the super enhancer was also tested and exhibited interaction with CTCF (Fig. 3B). E8 also shows CTCF occupancy on its genomic region (Fig. 2C). However, CTCF failed to interact with

BoxB RNA (viral RNA recognized by anti-terminator protein λN) (Fig. 3B). These observations were confirmed by another orthogonal technique UV-RIP which captures the binding of RNA and proteins *in vivo* (Fig. 3C).

Though, the CTCF occupancy was high on transcribing boundaries (Fig. 1D-E) but surprisingly, the CTCF motif was weakly present in these boundaries as compared to non-transcribing and random boundaries (Fig. 3D). This suggests that RNA may allow high affinity CTCF binding to less favourable CTCF motifs. This RNA aided CTCF occupancy was also evident from more number of CTCF peaks on transcribing boundaries (Fig. 3E) and more signal per peak (Fig. S6F). Similarly, higher peak per bp occupancy of CTCF on transcribing boundaries despite of them having weaker motif was seen on genic (Fig. 3F) and non-genic boundaries (Fig. 3G) with high RNA. These data suggest that presence of RNA can overcome the limitation of a weak CTCF motif and can assist in more numbers of CTCF binding events and with high affinity on genic and non-genic transcribing boundaries. Moreover, we did not notice any deviation of CTCF motif orientation at transcribing vs. non transcribing loop anchors (Data not shown) indicating, the observed effects are not related to CTCF orientation.

Next, we compared the stability, polyadenylation and splicing features of RNAs at TAD boundary with other RNAs. We compared genic transcripts arising from genic boundaries with other genic RNAs that are not within the boundaries. Similarly, transcribing non-genic boundaries show presence of enhancer like features (Gong et al., 2018; Sun et al., 2019) but the levels of K3K27ac, PolII, H3K4me3 are far less on these CTCF-bound regions within the boundaries as compared to active enhancers in general (Matthew and Waxman et al., 2018). However, it has been a standing question as to what is the role of these enhancer like regions that are rich in CTCF within the boundaries. Despite these different features of nested enhancers within the boundaries, the non-coding RNAs arising from these enhancer like regions are indeed eRNAs. Hence, we compared these non-coding RNAs with other eRNAs that are transcribed on enhancers but elsewhere in the genome. For turnover of RNA, we compared the ratio of nascent transcription with steady levels of these RNAs within the same experimental setting.

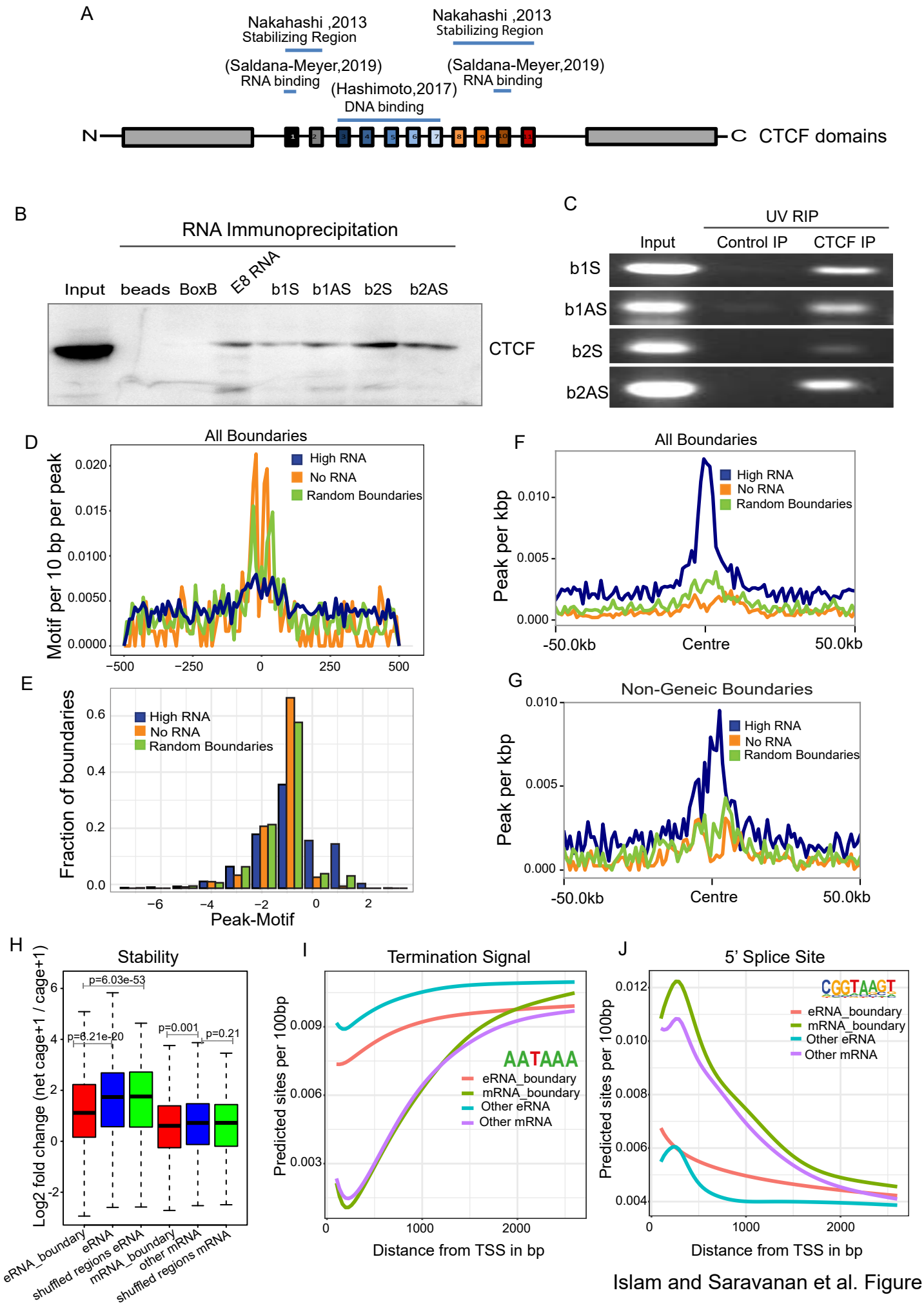

Islam and Saravanan et al. Figure 3

Figure 3. Non-coding RNAs and CTCF physically interact at 9p21 TAD boundary: A. Schematic showing CTCF domains and 11 zinc fingers. The blue lines indicate the reported regions important in its stabilization and RNA binding. **B.** Immunoblot for CTCF on RNA pulldowns performed on various RNAs (n=2). **C.** Agarose gel image showing the UV-RIP RT-PCRs for sense and anti-sense RNA arising from B1 and B2 CTCF sites (n=2). **D.** Line plots show the CTCF motif per 10 base pair per peak on various classes of boundaries. **E.** Fraction of boundaries with differential occupancy of CTCF peaks over the presence of the CTCF motif**. F.** CTCF peaks per kbp on all transcribing boundaries with high RNA, no RNAs and random boundaries (50 kb flanks on both side). **G.** CTCF peaks per kbp on non-genic transcribing boundaries with high bRNAs, no bRNAs and random boundaries. **H.** Log2FC of NET-CAGE+1/ CAGE+1, indicating stability of RNA at TSS identified from NET-CAGE at boundaries and TSS not at boundaries. b eRNA denotes the bRNA from non-genic boundaries, b mRNA denotes the mRNA from genic boundaries **I.** Average predicted TTS sites from the TSS identified in different classes of RNA by NET-CAGE. **J.** Average predicted 5'SS sites from the TSS identified by NET-CAGE. The p-values in boxplots were calculated by Mann Whitney test (Wilcoxon two-sided rank sum test). The boxplots depict the minimum (Q1-1.5*IQR), first quartile, median, third quartile and maximum (Q3+1.5*IQR) without outliers.

In general, eRNAs exhibit fast turnover as seen by higher ratio of nascent: mature RNA as compared to genic RNA (Fig. 3H) (Andersson et al. 2014). Interestingly, the genic RNA within boundaries were slightly more stable compared to other genic RNAs (Fig. 3H). Similarly, non-coding RNAs on non-genic boundaries exhibited lower ratio of nascent RNA: mature RNA as compared with eRNAs (Fig. 3H) suggesting, non-coding RNAs on non-genic boundaries are more stable as compared to eRNAs emerging from enhancers elsewhere. Perhaps, the stable nature of these RNAs is required for stable binding of CTCF at transcribing boundaries.

Next, we tested if the genic and non-genic RNAs are different in terms of transcriptional termination and 5' splicing sites compared to eRNAs and mRNAs that are transcribed elsewhere in the genome. As expected, the TTS was least present around the TSS of genic transcripts as compared to non-genic RNAs and eRNAs (Fig. 3I) but, non-genic RNAs on boundaries showed lesser enrichment of TTS as compared to eRNAs again pointing towards their stable nature (Fig. 3I). 5' splicing sites were under-represented in eRNAs and RNAs from non-genic boundaries compared to genic transcripts (Fig. 3J). Interestingly, RNAs from non-genic boundaries exhibited slight enrichment of splice sites compared to other eRNAs (Fig. 3J).

These data suggest that non-coding RNAs (eRNAs) from non-genic boundaries are more stable and exhibit less termination signal and more 5' splicing sites as compared to eRNAs elsewhere in the genome. Further, even the genic transcripts from genic boundaries exhibited more stability and 5' splice sites. Furthermore, these RNAs are transcribed at the CTCF-rich regions of boundaries. Thus, overall the RNAs from boundaries (coding or non-coding) have different features than other RNAs in the genome thus, we named them as bRNAs (Boundary-RNA).

TAD transcription is regulated by bRNAs

Next, we compared the transcriptional potential of the TADs with high, low, random non-transcribing boundaries and random boundaries and found that the transcriptional output of the entire TAD (Fig. 4A) or of the individual genes (Fig. S7A) was correlated with the levels of bRNAs at boundaries. This observation was found to be true on non-genic boundaries as well (Fig. S7B). This data shows that the presence of not only the genic RNA but also the non-genic RNAs at the

boundaries is positively correlated with high transcriptional activity of genes with in the TAD. We asked if this positive correlation is also exhibited as a result of high interactions between promoters and these boundaries. Towards this, we analysed the publicly available promoter capture-seq data in HeLa cells (Thiecke et al., 2020). The promoters exhibited higher interactions with boundaries of respective TADs as compared to random regions, suggesting that promoters tend to interact more with boundaries than expected (Fig. 4B). Further, we found that the genes that interacted with boundaries were relatively more active than genes that interacted with any other genomic regions (Fig. 4C). In order to test the generality of these observation, we asked if the transcribing boundaries in HeLa show open chromatin features (a proxy for active transcriptional potential) in cervical tumors in TCGA datasets. We observed a positive correlation between the level of bRNAs in HeLa and ATAC-seq signal on the same boundaries in cervical tumors (Fig. S7C). Further, the transcriptional status and overall ATAC-seq signal in these TADs was also proportional to bRNAs levels. (Fig. 4D-E). Together, these data suggest that transcribing boundaries tend to interact with promoters and are positively associated with the higher rate of TAD transcription.

Next, we confirmed the direct physical interaction between *CDKN2A* promoter and boundary regions by 4C-seq at *CDKN2A* promoter (Fig. 4F). We then asked if bRNAs play any direct roles in transcriptional activity of genes within this TAD. Interestingly, we observed downregulation of INK4a, ARF (Transcribed from *CDKN2A*), INK4b (Transcribed from *CDKN2B*) and MTAP expression upon shRNA mediated knockdown of both sense and anti-sense bRNAs at the B1 and B2 CTCF sites, whereas the transcription of DDX5 (non-INK4a/ARF TAD gene) remained unchanged upon these perturbations (Fig. 4G). These data suggest that *de novo* bRNAs positively regulate the transcription of the genes within the *INK4a/ARF* TAD where promoter physically interacts with TAD boundary.

However, the above observation cannot distinguish between the role of CTCF or bRNA *per se*, since the loss of bRNA also causes the loss of CTCF binding at the TAD boundary. Thus, we asked if loss of CTCF levels would also cause the gene repression. We observed downregulation of INK4a/ARF genes upon depletion of CTCF levels using pool of specific siRNAs (Fig. 4H-I) suggesting, bRNA and CTCF loss individually causes INK4a/ARF gene down regulation. However, global CTCF knockdown affect all CTCF bound regions within the TAD. Hence, the

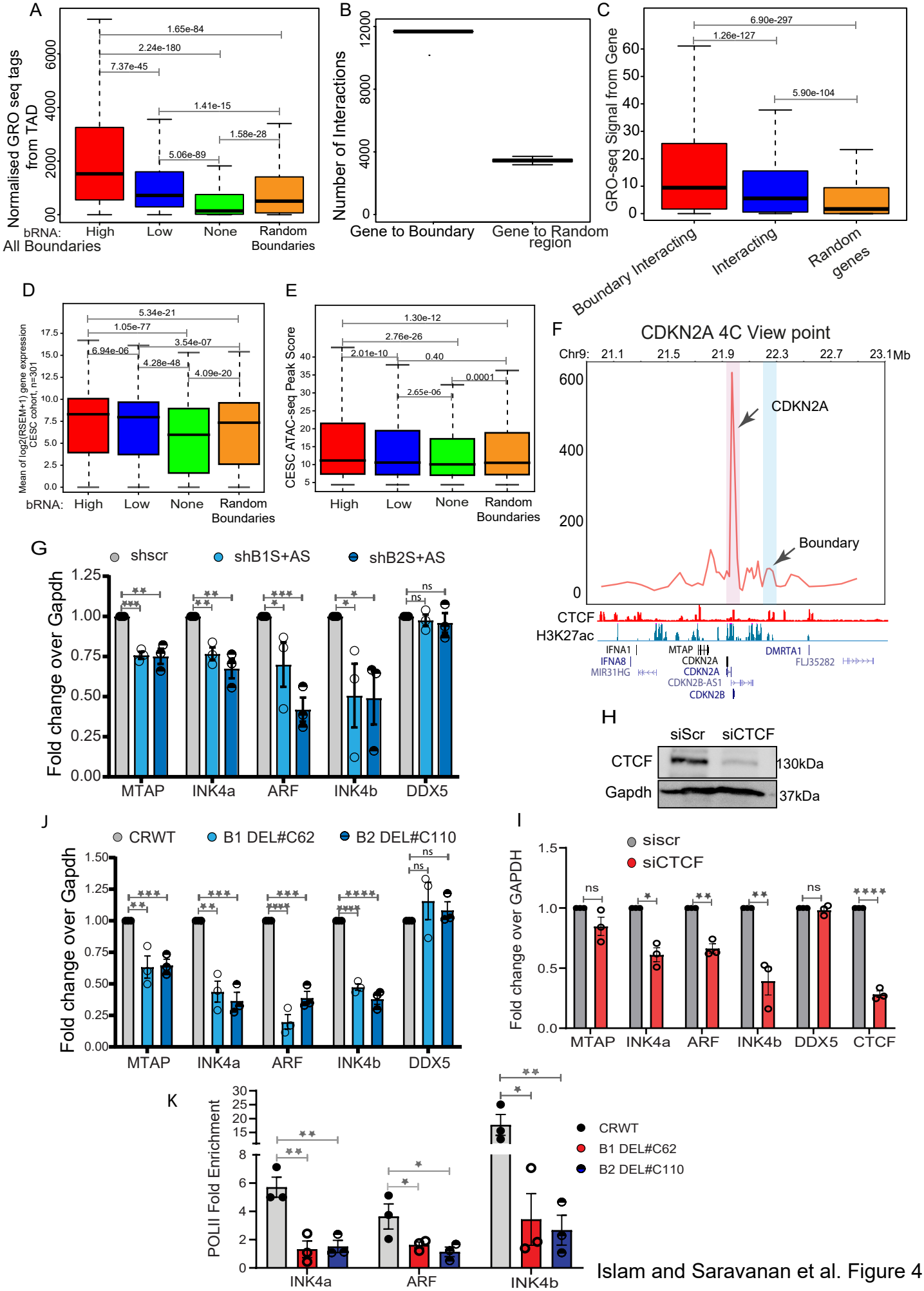

Islam and Saravanan et al. Figure 4

Figure 4. TAD transcription is regulated by bRNAs: A. Box plots showing GRO-seq tags from the entire TAD with high, low, non-transcribing and random boundaries. **B.** Graph showing the number of interactions between gene and; boundaries, and 100 randomizations of interactions between boundaries and random regions. **C.** Box plots showing the GRO-seq tag counts from genes when they interact with boundary or any region vs. random interactions. **D.** Box plots showing the RNA-seq expression of TADs with boundaries exhibiting different levels of bRNAs (HeLa) in Cervical Squamous Cell Carcinoma tumors from TCGA. **E.** Box plots showing the ATAC-seq signal of TADs with boundaries exhibiting different levels of bRNAs in Cervical Squamous Cell Carcinoma tumors from TCGA. **F.** 4C plot at CDKN2A promoter viewpoint, the interaction with boundary is highlighted in blue. The plot is overlaid with H3K27ac, CTCF and gene annotations in HeLa. **G.** qRT-PCR plot shows the change in gene expression upon shRNA mediated knockdowns of bRNAs arising from B1 and B2 CTCF sites at INK4a/ARF TAD boundary. **H.** Immunoblot showing the drop in CTCF protein levels upon its siRNA mediated knockdown. **I**. qRT-PCRs showing the down regulation of INK4A/ARF genes and levels of DDX5 and CTCF upon CTCF knockdown. **J.** qRT-PCR showing the changes in expression of different genes in INK4a/ARF TAD and DDX5 upon cas9 mediated independent deletion of B1 and B2 CTCF sites. **K.** PolII ChIP signal at INK4a, ARF and INK4b promoters in WT and in cells with B1 and B2 CTCF sites deletions. Error bars denote SEM from three biological replicates. *p*-values were calculated by Student's two-tailed unpaired *t*-test in **G, I, J** and **K.** ****$p < 0.0001$,***$p < 0.001$,**$p < 0.01$,*$p < 0.05$, $^{ns}p > 0.05$. p-values in boxplots were calculated by Mann Whitney test (Wilcoxon two-sided rank sum test). The boxplots depict the minimum (Q1-1.5*IQR), first quartile, median, third quartile and maximum (Q3+1.5*IQR) without outliers.

effects of other CTCF sites apart from B1 and B2 CTCF sites at boundary cannot be ruled out. To test the effects of loss of CTCF at the boundary only, we deleted the B1 and B2 CTCF sites individually in HeLa cells (Fig. S8A-B) and interrogated the expression of INK4a/ARF genes within the TAD. Similar to bRNA and CTCF knockdown, we observed the down regulation of these genes in boundary deleted cells (Fig. 4J). The downregulation of mRNA was also noticed at p16 protein levels upon both, bRNA knockdown and boundary deletion (Fig. S8C). Further, the loss of PolII at these promoters confirms the transcriptional inhibition of INK4a/ARF promoters (Fig. 4K). These data suggest that the bRNA mediated loading of CTCF at the boundary functionally regulates the expression of genes within the *INK4a/ARF* TAD.

Transcriptional activity of promoters does not regulate non-genic transcription at boundaries

bRNAs regulate *INK4a/ARF* TAD transcription but the question remains as to what causes the transcription of *de novo* bRNA at this boundary. We asked if the transcriptional activity of the *INK4a/ARF* promoters indeed causes the transcriptional activation at the boundaries of the same TAD. Towards this, we chose to delete the promoters of these genes using CRISPR tools however, HeLa cells are addicted to high levels of these proteins and do not survive without them (McLaughlin-Drubin et al., 2013; Pauck et al., 2014) hence, we could not obtain gene knockout single clones. Alternatively, we blocked the promoters (*CDKN2A*, *CDKN2B* and *MTAP*) via specific gRNAs and dCas9-KRAB (Fig. 5A) and tested the levels of bRNAs at B1 and B2 CTCF sites. We first confirmed the successful CRISPRi by observing the transcriptional down-regulation of these genes (Fig. 5B, red bars). Interestingly, the levels of bRNAs were unaffected upon such transcriptional inhibition of the promoters (Fig. 5B, blue bars). In concordance with unperturbed bRNA expression, we did not observe any change in CTCF occupancy at B1 and B2 CTCF sites but we observed the loss of CTCF on 5' boundary that overlaps with MTAP gene potentially due to down-regulation of *MTAP* gene (Fig. 5C). The boundary of flanking TADs also did not exhibit any perturbations in CTCF occupancy (Fig. 5C). These data suggest that bRNAs regulate the transcription of promoters in *INK4a/ARF* TAD but this transcriptional activity is not the cause of bRNA expression at the boundary.

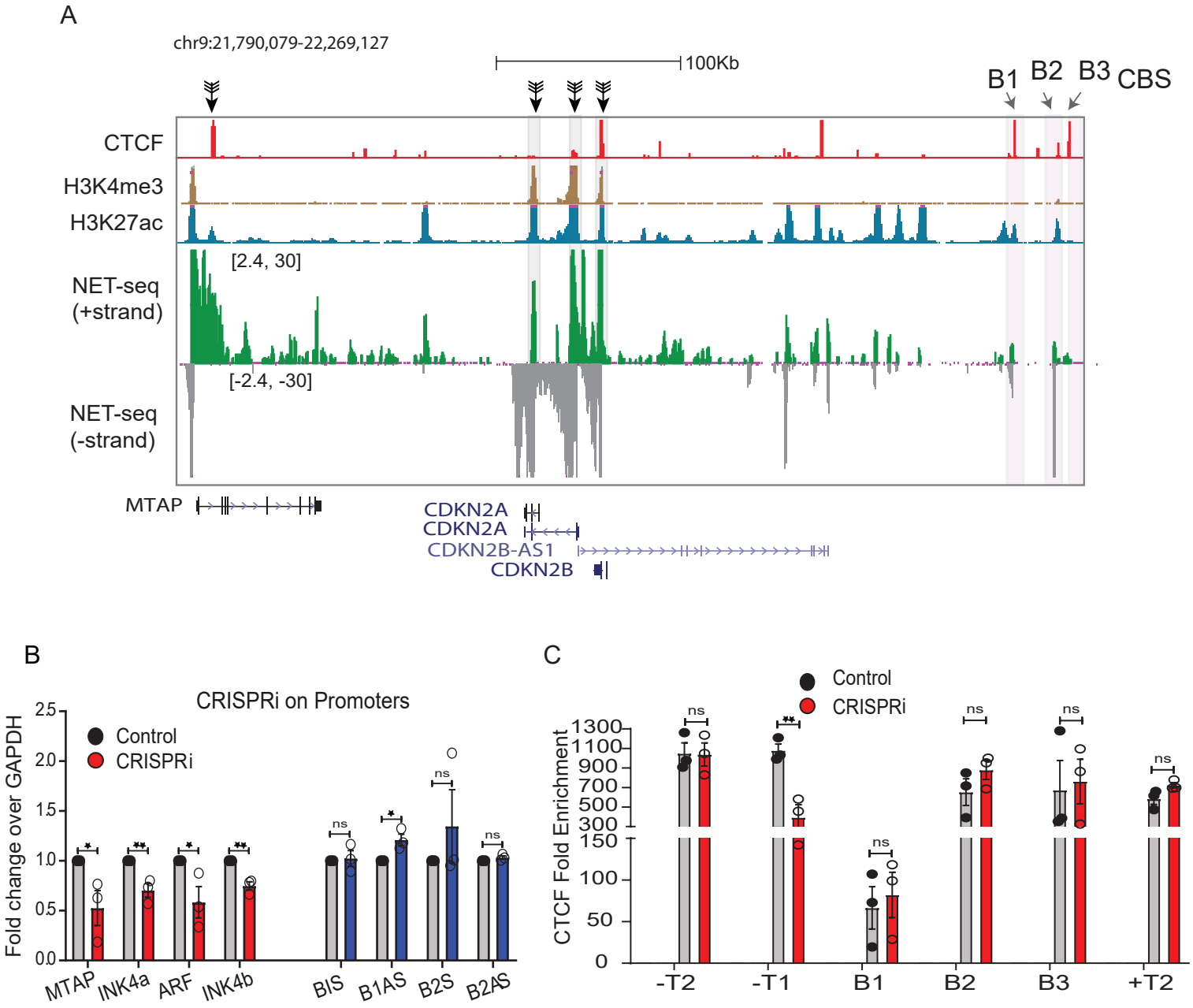

Islam and Saravanan et al. Figure 5

Figure 5. Transcriptional activity of promoters does not regulate *non-genic* transcription at boundaries: A. Browser shots displaying the promoters targeted by CRISPRi (Black arrows), the track is overlaid with CTCF, H3K4me3, H3K27ac and mNET-seq tracks. **B.** qRT-PCR assessing the changes in INK4a/ARF genes, sense and antisense bRNA arising from B1 and B2 CTCF sites upon CRISPRi on promoters. **C.** CTCF enrichment on boundaries of INK4a/ARF and its flanking TADs upon CRISPRi on INK4a/ARF promoters. Error bars denote SEM from three biological replicates. *p*-values were calculated by Student's two-tailed unpaired *t*-test in **B** and **C.** $^{**}p < 0.01$, $^{*}p < 0.05$, $^{ns}p > 0.05$.

bRNAs are positively regulated by enhancers within the TAD

Since, the transcriptional potential of TADs with transcribing boundaries (genic RNA and non-genic *de novo* RNA) was higher, we asked if the number of active enhancers in these TADs were also high to account for the active gene transcription. In agreement with high transcriptional levels of genes, these TADs were also enriched in total H3K27ac levels and number of H3K27ac marked enhancers (Fig. 6A and B). Notably, PolII enrichment was also high in accordance with the presence of high gene transcription and active enhancers in these TADs as compared to the TADs with non-transcribing boundaries and random boundaries (Fig. 6C). These observations were also true for non-genic boundaries (Fig. S9A-C). To test if there is a regulatory axis between enhancers and bRNA expression at *INK4a/ARF* TAD, we used series of lines with active enhancer deletions within the super enhancer (E8, 12 and 17) (Fig. 6D, Farooq et al., 2021). The enhancer cluster contains 21 enhancers and down-regulation of *INK4a/ARF* genes was observed by RNA-seq in these deleted lines (Fig. 6E) (Farooq et al., 2021), confirming that these enhancers are functional enhancers. We then asked if these enhancers indeed regulate the boundaries as well. Interestingly, we noted the down-regulation of sense and anti-sense bRNAs at the B1 and B2 CTCF sites upon E8, E12 or E17 deletions (Fig. 6F) suggesting, enhancers indeed transcriptionally activate *de novo* bRNAs at the boundary region. Further, we performed 4C on an enhancer beside E8 enhancer as a viewpoint. As expected, we observed strong interaction of this enhancer with other enhancers in the super enhancer cluster including E8. We also noted its interactions with *CDKN2A* and *CDKN2B* promoters and with the boundary region (Fig. 6G, right highlighted pink). Intriguingly, we observed the loss of SE interaction with the boundary and the promoters upon deletion of the E8 enhancer (Fig. 6G). Such interactions between boundaries and enhancers are reported in literature (Sun et al., 2019) but it is unknown if they have any regulatory relation. These data suggest that apart from activating their target promoters, functional enhancers positively regulate the transcription at the boundaries by direct interactions. To test if high levels of bRNAs and enhancer activity insulate the boundary better *in vivo* we further interrogated the INK4a/ARF TAD upon senescence where TAD gains more activation transcriptionally due to the cell cycle regulatory roles of this locus. We analyzed publicly available data on proliferative and senescent fibroblasts (replicative senescence). Data suggests that upon senescence, the bidirectional eRNA expression increases by many folds on the super enhancer cluster (Fig. S10A, blue highlighted

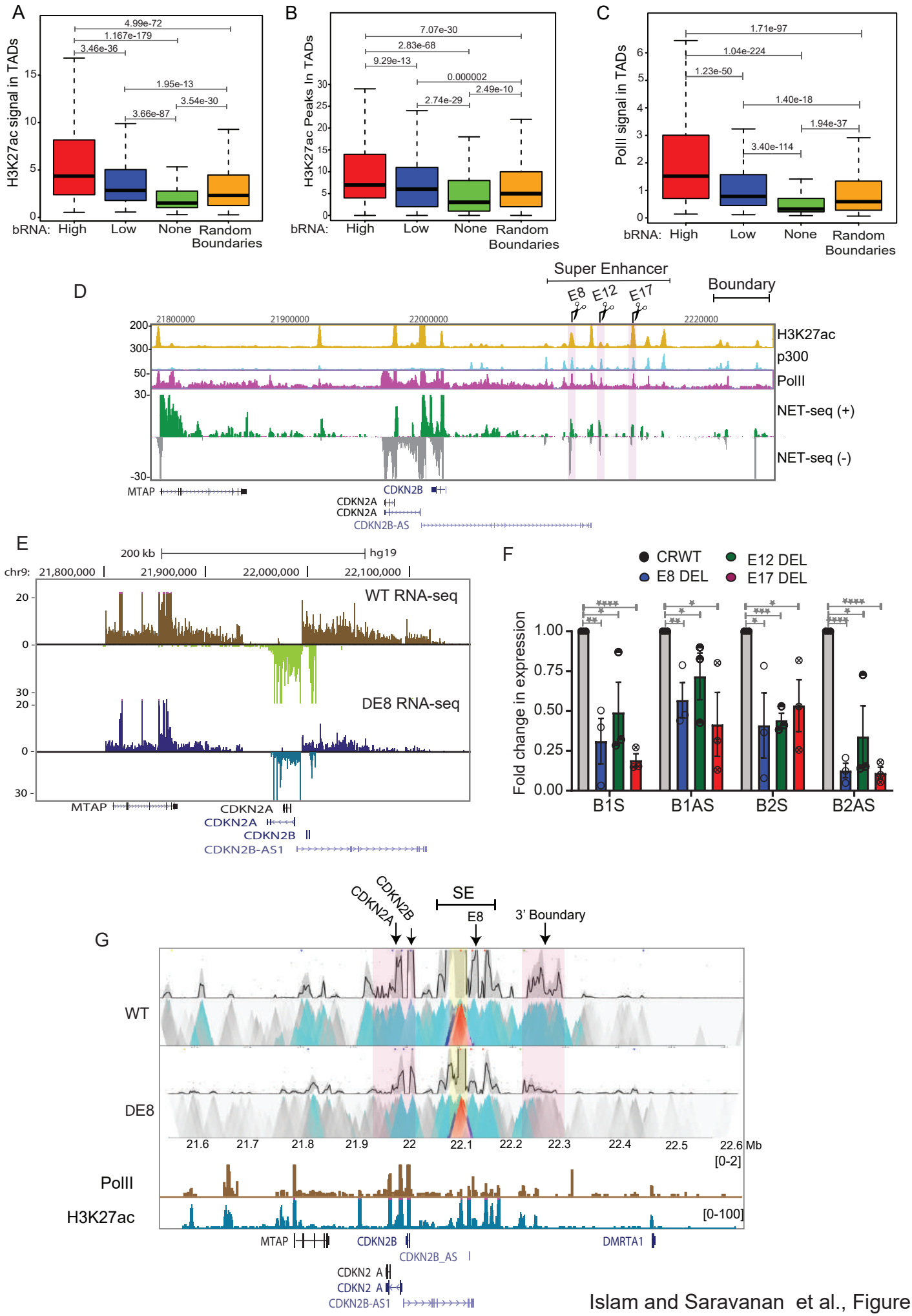

Islam and Saravanan et al., Figure 6

Figure 6. bRNAs are positively regulated by enhancers within the TAD: A. Boxplots displaying enrichment of H3K27ac in TADs with high, low, non-transcribing and random boundaries. **B.** Boxplot showing number of H3K27ac peaks in TADs with various boundaries. **C.** Levels of PolII in TADs with different boundaries. **D.** UCSC browser shot showing H3K27ac, p300, PolII ChIP-seq and mNET-seq on INK4a/ARF TAD. The tracks are overlaid by the gene annotations. The highlighted regions represent the enhancers (E8, E12 and E17) that were deleted. **E.** browser shot shows RNA-seq at INK4a/ARF TAD in WT and E8 enhancer delete line. **F.** qRT-PCR shows levels of sense and antisense bRNA arising from B1 and B2 CTCF sites upon E8, E12 and E17 enhancer deletions. **G.** 4C-seq plot in WT and in E8 deletion line on an enhancer beside E8 enhancer as a viewpoint (Yellow highlight) exhibiting interactions with promoters and 3' boundary region (Pink highlight). The interaction heatmap is overlaid by PolII, H3K27ac ChIP-seq tracks and gene annotations. Error bars denote SEM from three biological replicates. *p*-values were calculated by Student's two-tailed unpaired *t*-test in **F.** ****$p < 0.0001$,***$p < 0.001$,**$p < 0.01$,*$p < 0.05$. p-values in boxplots were calculated by Mann Whitney test (Wilcoxon two-sided rank sum test). The boxplots depict the minimum (Q1-1.5*IQR), first quartile, median, third quartile and maximum (Q3+1.5*IQR) without outliers.

region). The INK4a/ARF gene expression and the bRNA expression also increases under this scenario (Fig. S10A, pink highlighted region). We validated the gain of gene transcription, bRNA expression and CTCF enrichment at the boundary upon X-ray induced senescence (non-replicative senescence) (Fig. S10B-D) and the elevated p16 and p21 protein levels (Fig. S10E). Using HiC data, we then observed the gain of intra-TAD interactions at this TAD in senescent cells as compared to proliferative cells (Fig. S10F). Together these data suggest that as the enhancers gain more activity, they interact with boundaries to induce bRNA expression. The induced bRNA in turn recruits more CTCF to increase the insulation.

bRNAs provide better insulation to favour robust enhancer:promoter interactions

Enrichment of CTCF at boundary regions is an indicator of a better insulated boundary and due to the better insulation, enhancers are contained within respective TADs. Since, the levels of CTCF and insulation score was high on transcribing boundaries thus, we asked if the enhancer and promoter interactions were stronger within the TADs of transcribing boundaries vs. non-transcribing boundaries. Interestingly, we observed relatively higher strength of enhancer:promoter interactions in these TADs as compared to the TADs with non-transcribing boundaries (Fig. 7A-B). Further, since bRNA knockdown reduced the CTCF occupancy at the boundary and also the transcription of genes was downregulated in the *INK4a/ARF* TAD (Fig. 2, 4), we asked if the insulation of this TAD and SE:promoter interactions were also affected upon bRNA depletion. Towards this, we performed 4C assays at enhancer viewpoint upon knockdown of sense and anti-sense bRNAs at the B1 CTCF site. Not surprisingly and in concordance with CTCF levels loss, we observed the loss of boundary: enhancer interactions (Fig. 7C). Importantly, we observed the weakening of enhancer: INK4a/ARF promoter interactions as well. Further, the enhancers gained interactions with the +1 TAD boundary indicating that the enhancer was now able to interact with the boundary of the next TAD (Fig. 7C). Intriguingly, we also observed the gain of CTCF at +T1 boundary upon bRNA depletion (Fig. 2F). Then to test if these inter-TAD interactions were indeed indicative of loss of boundary functions, we extended the 4C on the same enhancer viewpoint in cells with B1 CTCF site deletion. We noted a similar loss of enhancer: promoter and enhancer: boundary interactions and gain of interactions with +T1 boundary region

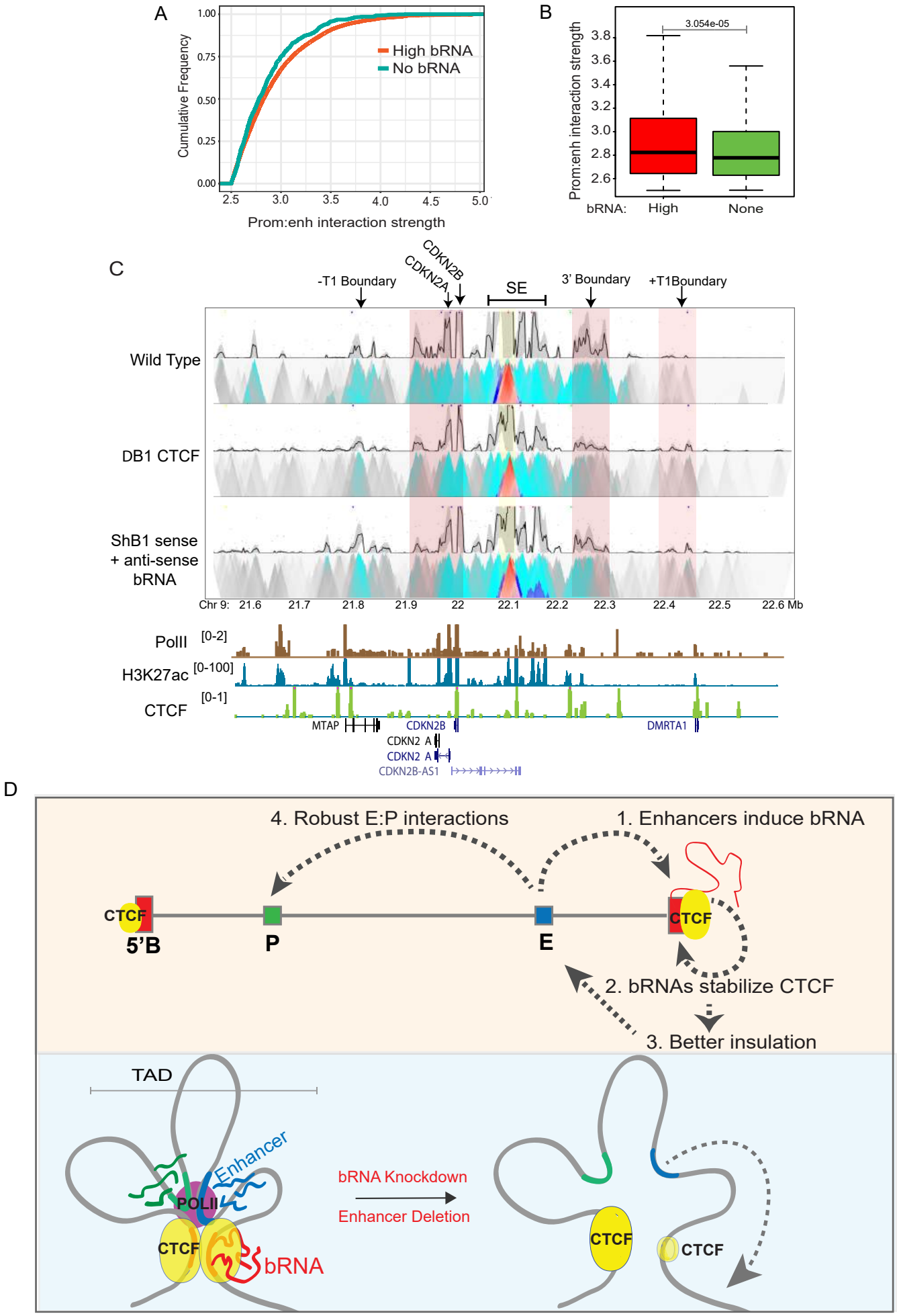

Islam and Saravanan et al. Figure 7

Figure 7. bRNAs provide better insulation to allow robust enhancer:promoter interactions: **A.** Cumulative frequency of the interaction strength between enhancer and promoters interacting with boundaries showing high and no transcription. **B.** Enhancer:promoter interaction strength within TADs with high and non-transcribing boundaries. **C.** 4C-seq plot on region beside E8 enhancer as a viewpoint (Yellow highlight) in WT and upon B1 CTCF site deletion (ΔB1) and knockdown of B1 sense and anti-sense bRNAs. The anchored region exhibiting interactions with promoters and 3' boundary region and +T1 boundary (Pink highlights). The interaction heatmap is overlaid by PolII, H3K27ac and CTCF ChIP-seq tracks and gene annotations. **D.** Model depicting that: 1. Active enhancer physically interacts with boundary and activates the bRNA transcription at the boundary. 2. The bRNA in return stabilizes the CTCF at these boundaries thereby, 3. The insulation of these TADs is strengthened. 4. This favors intra-TAD enhancer: promoter interactions to facilitate robust gene transcription. The loss of bRNA/enhancer deletion reduces the bRNA levels which triggers the loss of CTCF and insulation of TADs. Enhancer:promoter interactions weaken in these scenario which causes concomitant loss of gene transcription. Kolmogorov–Smirnov two-sided test was used to calculate significance in (A). p-values in boxplots were calculated by Mann Whitney test (Wilcoxon two-sided rank sum test). The boxplots depict the minimum (Q1-1.5*IQR), first quartile, median, third quartile and maximum (Q3+1.5*IQR) without outliers.

(Fig. 7C). This data confirms that bRNA loss weakens the insulation of the TAD which is similar to boundary loss (Fig. 7D).

Discussion

RNaseA treatment followed by HiC shows the perturbations in 3D chromatin architecture suggesting, the RNA is an integral player in chromatin organization (Barutcu et al., 2019). Further, genome organizer CTCF interacts with RNA and mutations in its RNA binding ZF1 and ZF11 exhibit weakening of TADs favoring more inter-TAD interactions (Hansen et al., 2019; Saldaña-Meyer et al., 2019). However, these experiments have not provided the identity of RNA and its transcribing sites that are important in such chromatin organization roles. Towards this, transcription at TAD boundaries is speculated to regulate TAD functions (D. Zhang et al., 2020; Zhang et al., 2019). Here we show that bRNAs emerging at TAD boundaries (from genes overlapping with boundary or *de novo* non-coding transcripts) have a direct role in CTCF recruitment at these boundaries and therefore in TAD strength and gene regulation. Our data, provide the direct evidence that indeed bRNAs at boundary create insulated neighbourhood by the virtue of binding with CTCF that favours enhancer:promoter interactions for robust gene activation thus, bRNAs at boundaries make genome topology less “hardwired” and more regulated.

Using a series of enhancer and CTCF sites deletions at INK4a/ARF TAD, we observed that enhancers interact and positively regulate the expression of bRNA (gene transcripts or non-coding RNAs) at TAD boundaries. bRNAs in turn stabilizes the binding of CTCF at the boundary, in particular on weak CTCF motifs (Fig. 3D). These boundaries show more number of CTCF peaks (Fig. 3E-F) and hence, the TAD boundary is better insulated. With these CTCF features, perhaps, bRNA transcribing boundaries with multiple CTCF peaks do not let cohesin ring slip to the next TAD (Hansen, 2020; Kentepozidou et al., 2020) thereby insulation is enhanced. Any RNA perhaps would aid in CTCF recruitment in neighbouring regions if CTCF motif is present and for these reasons, the transcription and CTCF occupancy need not occur at the same genomic coordinate as the presence of RNA in surroundings would aid in CTCF recruitment. However, the transcription sites due to high levels of overall RNA in surroundings would do this efficiently.

Further, slower turnover rate of bRNAs would be imperative for stable TAD organization. We would hypothesize that either the stable bRNA directly allows for better recruitment of CTCF or that the stability of RNA is a function of its association with the boundary. RNA:CTCF interactions could keep both RNA and CTCF stable for longer at the regions of higher local RNA concentration. Towards this, perhaps eRNAs within the boundaries are repurposed as bRNAs for these added functions.

During development or signaling cues when enhancers are activated, the weaker CTCF sites if divergent may act as a stronger boundary by the virtue of bRNA and may thereby stabilize the dynamic chromatin changes that are the result of enhancer activation in these TADs giving rise to differential gene regulation. For example, we observed higher insulation of INK4a/ARF TAD upon onset of senescence where the TAD transcription is induced and coincides with the gain of enhancer functions and bRNA expression at the TAD boundary (Fig. S10A, F).

The bRNA loss reduces the enrichment of CTCF at the boundary and shows concomitant loss of enhancers and promoter interactions at INK4a locus (Fig. 2F, 7C). Whereas, interactions between these enhancers and the boundary (+T1) of neighbouring TAD strengthen, this gained looping also enhances the CTCF enrichment at +T1 (Fig. 2F, 7C) suggesting, the insulation of INK4a/ARF boundary upon bRNA perturbations is reduced. These data indicate that bRNAs stabilize CTCF at the boundary thus, interactions between the genes within these TADs and their cognate enhancers is favored resulting in robust transcription of genes due to better insulation of these TAD boundaries. These results contrast the observations that deletion of boundary had no effect on E-P interaction (Yokoshi et al., 2020) but agree with other literature (Arzate-Mejía et al., 2020).

Transcriptional inhibition also affects the chromatin interactions. This could arise from RNA *per se* or from the PolII and its associating machineries that occupy the enhancers and promoters. Towards this, we used CRIPSRi that not only inhibits the transcription thereby the transcripts but also inhibits the binding of PolII machinery. Interestingly, CRISPRi mediated active silencing of TAD did not alter the expression of bRNA and thereby CTCF occupancy at the boundary (Fig. 5 B-C) suggesting that neither transcriptional activity of promoters or the alterations in the PolII machinery, directly change the bRNA mediated insulation of boundary. Thus, the effects on

genome organization upon transcription inhibition perhaps do not arise from the promoters. Our data suggests that observed effects on TAD topology upon transcription inhibition could arise from inhibition of enhancer transcription thereby its activity which can alter the boundary functions leading to compromised TAD insulation as seen by the loss of bRNA and super enhancer-boundary interactions upon deletion of E8 enhancer in INK4a/ARF TAD (Fig. 6F-G).

These observation are in agreement with the fact that TADs with super enhancers exhibit stronger boundaries (Gong et al., 2018; Sun et al., 2019). This is also evident by the presence of more number of enhancers in TADs with bRNA transcribing boundaries (Fig. 6A-B and S9A-B). The data indicates that as the TAD acquires enhancer activity, the enhancers loop with boundary to activate the bRNA expression. Then, the boundary insulates the TAD better thereby enhancers stably engage with the cognate promoters. The transcription assisted TAD boundary strengthening also corroborates with the observed zygotic activation dependent boundary formation (Hug et al., 2017) and in X chromosome inactivation (Giorgetti et al., 2016). Further, a combination between CTCF site at the boundary and active enhancers are required to induce bRNA-dependent insulated boundary. This suggests that mere activation of transcription at the boundary is not sufficient to create the TAD boundary (Bonev et al., 2017; Hug et al., 2017). Together, these results show that active enhancers directly mediate better insulation of TADs by activating the transcription at TAD boundaries which favours robust intra-TAD enhancer:promoter interactions to activate the gene transcription.

The boundaries per se also harbor H3K27ac and PolII marked regions suggesting the presence of active regulatory elements at these boundaries (Gong et al., 2018; Sun et al., 2019; Hsieh et al., 2020; Matthew et al., 2018). The *de novo* RNA (bRNA) that emerges from these regions tend to be bidirectional resembling the bi-directional nature of eRNAs emerging from functional enhancers (Li et al., 2016, 2013). The strong CTCF binding along with DNA structural features at these active regions in boundaries may give these elements a structural and functional ability that is different from CTCF-bound enhancers therefore, these boundaries functionally behave differently. Nonetheless, CTCF binding, insulation at the boundaries and enhancer:promoter interactions in TADs corresponds to the bRNA levels (Fig. 1D-E, F and Fig. S1) suggesting the

RNA (from genes or from regulatory elements within boundaries) potentially determines the strength of these boundaries.

Limitations of the study:

While our study provides bRNA as the additional layer that determines the boundary insulation, the other players such as transcription factors and DNA sequences that augments the insulation function of TAD boundaries are to be uncovered. The role of the dynamics of RNA with cohesin has not been probed in this manuscript but may add to the above mentioned mechanism. Further, apart from binding with CTCF, if the stable nature of bRNAs provide any added function over eRNAs elsewhere remains to be studied.

Acknowledgements: We thank Tapas K. Kundu for the discussions. We are grateful to Henrietta Lacks and to her family members for their contributions to biomedical research. We acknowledge support of the Department of Atomic Energy, Government of India, under project no.12-R&D-TFR-5.04-0800 and intramural funds from NCBS-TIFR (to DN and RS). DN is an EMBO Global Investigator. We also acknowledge the funding support from Welcome-IA: IA/1/14/2/501539 (to DN). UF is supported by CSIR (Govt. of India) senior research fellowship. KW and RM are supported by the TIFR-NCBS graduate program. KW is also supported by the CSIR-SPM (Govt. of India) fellowship.

Contribution: We thank the members of DN lab for comments and discussion on the manuscript. The study was conceived and designed by ZI, BS and DN. BS performed NGS data analysis. Most experiments were performed by ZI with help from UF and KW. AKS and RS executed tumor dataset analysis. JT performed CTCF Cut & Run. RNaseA experiment in SH lab. AP performed NGS library preparation and sequencing. DN, ZI and BS wrote the manuscript with inputs from all the authors.

Materials and Methods:

Cell Culture:

HeLa cells were obtained from ATCC and were cultured in (DMEM) Dulbecco's Modified Eagle's medium supplemented with 10% Fetal Bovine Serum and 1% Penicillin/Streptomycin. The cells were maintained at 37°C in presence of 5% CO_2 in a humidified incubator

Chromatin Immunoprecipitation:

Cells were crosslinked with 1% formaldehyde at room temperature for 10 mins with constant shaking. Glycine was added to a final concentration of 125 mM to quench the formaldehyde. Cells were washed three times with 1X ice cold PBS then were scraped and pelleted down 1X PBS at 4 ^{o}C. Cells were gently resuspended in nuclear lysis buffer (50 mM Tris-HCl pH 7.4, 1% SDS, 10 mM EDTA pH 8.0) supplemented with 1X PIC and incubated on ice for 10 mins. Lysate was subjected to fragmentation using Diagenode Bioruptor Pico for 20 cycles (30 s ON and 30 s OFF) to generate fragments of around ~500 bp. Cell lysate was cleared at 12K rpm for 12 mins. 100 ug of sheared chromatin was taken for each IP. The lysates were diluted by adding Dilution Buffer (DB) (20 mM Tris-HCl pH 7.4, 100 mM NaCl, 2 mM EDTA pH 8.0, 0.5% Triton X-100) supplemented with 1X PIC in 1:1.5 ratio (1 volume of sheared chromatin and 1.5 volumes of Dilution Buffer). 1 ug of antibody was added to immunoprecipitate the DNA and incubated on a rocking platform overnight at 4°C. 15ul of Pre-blocked (with 1% BSA) Protein G dynabeads (10004D, Invitrogen) were added to the tubes and rotated for 4h at 4 °C. Beads were collected, flow through was discarded and the samples were washed with Wash Buffer I (20 mM Tris-HCl pH 7.4, 150 mM NaCl, 0.1% SDS, 2 mM EDTA pH 8.0, 1% Triton X-100) at 4 ^{o}C on a rocking platform. Washings were sequentially repeated with Wash Buffer II (20 mM Tris-HCl pH 7.4, 500 mM NaCl, 2 mM EDTA pH 8.0, 1% Triton X-100), Wash Buffer III (10 mM Tris-HCl pH 7.4, 250 mM LiCl, 1% NP-40, 1% Sodium Deoxycholate, 1 mM EDTA pH 8.0 and 1X TE (10 mM Tris pH 8.0, 1mM EDTA pH 8.0). Chromatin was eluted with 200 ul of Elution Buffer (100 mM NaHCO3, 1% SDS) for 30 mins at 37°C in a thermomixer. The supernatant was collected in separate tubes and 14 µl NaCl (5 M) was added to eluted samples and kept at 65 °C overnight for de-crosslinking. Immunoprecipitated DNA was purified by Phenol:chloroform:isoamyl alcohol, followed by ethanol precipitation. The final air dried DNA pellet was dissolved in 100 ul of 1X TE. These samples were then used for qRT-PCRs using SYBR Green. Mean values for all the regions analyzed in different conditions were expressed as fold-enrichment compared over beads.

Statistically significant differences between different conditions were computed using a ***T*-test** (*p*-value < 0.05), ChIP primers are listed in Supplementary Table. 1.

RNA Isolation and cDNA synthesis:

Cells were lysed in 1 ml of Trizol (Thermo Fisher Inc.). 200 ul chloroform was added to the sample, briefly vortexed and centrifuged at 12K rpm for 12 mins. The aqueous phase was carefully collected and transferred to the fresh tube. 1 volume of isopropanol was added to the sample and incubated at room temperature for 10 mins to precipitate the RNA. The samples were centrifuged at 12K rpm for 12 mins, supernatant was discarded without disturbing the pellet. The pellet obtained was washed with 75% ethanol. Pellet was air dried and dissolved in RNase free water. RNA obtained was treated with ezDNase (Invitrogen) to remove the traces of contaminating DNA. 1 μg of RNA was used for each cDNA synthesis reaction by Superscript IV (Invitrogen) and random hexamers as per manufacturer's recommendation. The CFX96 touch (Biorad) real time PCR was used for qRT-PCRs. qRT-PCRs were performed using three biological replicates for each sample. The fold changes were calculated by the ΔΔCt method and individual expression data was normalized to GAPDH mRNA. The *p*-values were calculated by Student's unpaired two-tailed *t*-test. qRT-PCR primers are listed in Supplementary Table 1.

CRISPR Cas9 mediated deletion:

gRNAs were designed with crispr.mit.edu tool. gRNAs were selected based on the highest score and a least number of off targets. All the gRNAs were cloned in pgRNA humanized vector (Addgene #44248) (a gift from Stanley Qi Lab) between BstX1 and Xho1 restriction sites. gRNAs were co-transduced with lenti-Cas9 vector. Cells were put under selection using puromycin (3ug/ml) for 48 hours. Single cells were seeded in a 96 well plate. Wells with single cells were marked and allowed to grow till they formed colonies. The cells were trypsinzed and shifted to 48 well plates and allowed to grow to confluence and then half of the cells were taken for the surveyor assay and the other half was plated again. Surveyor assay was carried out by PCR based method using primers listed in the Supplementary Table 1.

CRISPRi: gRNA design and cloning:

We used gRNA design tool (https://portals.broadinstitute.org/gpp/public/analysis-tools/sgrna-design) to design the gRNAs against TSS of *MTAP*, *CDKN2A* and *CDKN2B* in the INK4a/ARF TAD. For each gene, two gRNAs were designed. The gRNAs were cloned in a customized PX459 vector (pSpCas9(BB)-2A-Puro V2.0, Addgene # 62988) was a gift from Feng Zhang lab. The Cas9 enzyme cassette was removed from PX459 by digesting it with Xba1 and Not1 followed by blunt end ligation. The cloning of the gRNAs in the customized PX459 plasmid was performed as per the Zhang Lab's general cloning protocol. dcas9 plasmid along with gRNA specific to genes were transfected in 70% confluent cells. Transfections were done using Lipofectamin 2000 (Invitrogen, cat no# 11668027), CRISPRi cells were harvested for ChIP and gene expression analysis.

Lentiviral transduction:

HEK293FT cells were grown in poly-D lysine coated culture dishes. These cells were co-transfected with lentiviral packaging plasmids like VSVG a gift from Bob Weinberg (addgene #8454); PAX2 a gift from Didier Trono (addgene #12260) along with the plasmid of interest using Lipofectamine 2000 Invitrogen (cat# 11668027). Media was changed after 6 hours. Viral soup was collected after 48 h and 72 hours, pooled together, filtered with 0.44µm syringe filter and then finally added to cells along with 8ug/ml of polybrene. Transduction was stopped after 16 hours.

RNA Immunoprecipitation:

For RNA, primers were designed to amplify desired genomic regions that correspond to peak of bRNA (GRO-seq) at B1 and B2 CTCF sites of TAD boundary. The amplified products were cloned in pcDNA3 BoxB a gift from Howard Chang (Addgene #29729) plasmid. All the clones were confirmed by sanger sequencing, and subsequently used for RNA synthesis using T7 RNA polymerase (Promega Inc. P207e) and biotin RNA labeling mix (Roche11685597910). Primer sequences are mentioned in the Supplementary Table 1.

RNA immunoprecipitation was adopted from (Jayani et al., 2017), with some modifications. HeLa cells were grown to 90–95% confluency and were harvested by scraping and washed twice with

ice cold 1X PBS to gently resuspend in 2 ml of PBS. 2 ml of nuclear isolation buffer (NIB)(40 mM Tris–HCl (pH 7.5), 20 mM MgCl2, 1.28 M sucrose, 4 % Triton X-100, 1 mM PMSF, protease inhibitors, and 20 U/ml SUPERase inhibitor (Thermo Fisher Scientific, catalog # AM2694) was added and the pellet was gently resuspend. Then, 6 ml of distilled water was added and kept on ice for 20 min with intermittent gentle shaking. Nuclei were Pelleted by centrifugation at 2500×*g* for 5 min at 4ºC. The pellet was resuspended in 1 ml of RIP buffer (25 mM Tri–HCl (pH 7.4), 150 mM KCl, 0.5 mM DTT, 0.5 % NP40, 1 mM PMSF, protease inhibitors, and 20 U/ml SUPERase inhibitor) and incubated on ice for 5 min. Nuclei were sheared by 10 cycles of sonication (30s on and 30 s off, bioruptor) followed by centrifugation at 12K rpm for 10 min at 4ºC. 1 µg of biotinylated RNA was incubated with 20 µl of RNA structure buffer (RSB) (10 mM Tris–HCl (pH 7.0), 100 mM KCl, 10 mM $MgCl_2$, 1 mM PMSF, protease inhibitors, and 20 U/ml SUPERase inhibitor) at room temperature for 5 min. Folded RNA was mixed with 1 mg of nuclear extract in 500ul of RIP buffer and rotated at 4^0C for 1h. 15 ul of DynabeadsMyOne Streptavidin beads were added and rotation continued for one more hour. Samples were washed 3 times with RIP buffer and beads with proteins were boiled in 2XSDS for 10 min. Immunoblotting for CTCF was performed using the CTCF antibody (cell signaling, 3418).

UV RIP:

Ultraviolet-RNA Immunoprecipitation was performed as in (Rahnamoun et al., 2018) with some modifications. Hela cells at confluency of 80–90% were crosslinked by UV irradiation in Stratalinker UV cross-linker. Cells were washed three times with cold 1XPBS and scraped in PBS before subjecting to centrifugation at 2500 rpm. Pellet was lysed in RIP lysis buffer (25 mM HEPES-KOH at pH 7.5, 150 mM KCl, 0.5% NP40, 1.5 mM $MgCl_2$, 10% glycerol, 1 mM EDTA, 0.4 U RNase inhibitor (Invitrogen, 18091050), and 1X protease inhibitor cocktail (PIC) on ice for 30 min. Cleared cell lysates were subjected to IP with CTCF antibody bound Protein G Dynabeads (Invitrogen, 10004D) overnight. Samples were subsequently washed three times with RIP lysis buffer and RNA samples were eluted using TRIzol reagent. Prior to cDNA synthesis RNA was treated with RNase-Free DNase Qiagen (cat no.79256) to remove the traces of contaminating DNA. cDNA was prepared using random hexamers by Superscript IV (Invitrogen 18091050) as

per manufacturer's recommendation and analyzed by PCR primers listed in Supplementary Table 1 and were run on 1% Agarose gel.

Cell Fractionation:

Cell fractionation and RNAseA treatment of nuclei was adapted from (Gagnon et al., 2014). Briefly, cells were washed three times with cold 1XPBS and scraped in 1ml of PBS, pelleted down at 2500 rpm for 5 min at 4^0C. Pellet was then resuspended in Hypotonic Lysis Buffer (HLB)(10mM Tris HCl pH 7.5, 10mM NaCl, 3mM MgCl2, 0.3% NP-40, 10% glycerol, 1XPIC), the mix was incubated on ice for 10min and then centrifuged at 800g for 8min at 4^0C. The supernatant was transferred to a new tube and marked as Cytoplasmic fraction. The nuclei pellet after centrifugation was washed twice with HLB and centrifuged at 200g for 2 min at 4^0C. The pellet was then resuspended in 700 ul of ice cold Modified Wuarin-Schiebler buffer (MWS)(10 mM Tris-HCl (pH 7.5), 300 mM NaCl, 4 mM EDTA, 1 M urea, 1% NP-40, 1% glycerol,1XPIC) with or without 0.1ul of 100mg/ml RNaseA (Qaigen cat no 19101) for 15min on ice briefly tapped few times during incubation time and then centrifuged at 1000g for 5min at 4^0C. The supernatant was collected as a nucleoplasmic fraction. The chromatin pellet was washed twice with MWS buffer and centrifuged at 500g for 3min at 4^0C. The pellet was then dissolved in 500ul of Nuclear Lysis Buffer (NLB) (20mM Tris HCl ph 7.5, 150mM KCl, 3mM MgCl2, 0.3% NP-40, 10% glycerol,1XPIC) and sonicated for 10 cycles with (30 s ON, 30 s OFF) in Bioruptor (Diagenode). SDS loading dye was added and the samples were boiled before immunoblotting.

Chromatin associated RNA isolation:

Chromatin associated RNA isolation was adapted from (Conrad T et al., 2017). Trypsinized cells were collected in 1.5ml tubes and washed twice with 1xPBS and pellet down at 200xg for 2 min. To each pellet was added 400ul of Cell lysis buffer(10mM Tris HCl ph7.4, 150mM NaCl, 0.15% Igepal), gently pipetted 3-5times and then incubated for 5min on ice. To the Lo-bind 1.5ml tube was added 1ml(2.5 volume) of the cold sucrose buffer(10mM Tris HCl ph7.4, 150mM NaCl, 24% Sucrose) and gently overlaid with the cell lysate. Centrifuged at 3500xg for 5min,to collect the nuclear pellet. Isolated nuclei were rinsed with 1ml of ice cold 1xPBS-

EDTA solution followed by short spin at 3500xg. The nuclei were resuspended in 250ul of glycerol buffer(20mM Tris HCl ph7.4, 75mM NaCl, 0.5mM EDTA ph8.0, 50% Glycerol and then immediately was added 250ul of Urea buffer(10mM Tris HCl ph7.4, 1M Urea, 0.3M NaCl, 7.5mM MgCl2, 0.2mM EDTA,1%Igepal). Mixed with vortexing for 4s and then incubated on ice for 2min. Centrifuged at 13000xg for 2min to precipitate the Chromatin-RNA complex, the chromatin-RNA pellete was washed with 1xPBS-EDTA once and RNA was isolated using Trizol Reagent. RNA obtained was treated with ezDNase (Ambion) to remove the traces of contaminating DNA. 1 μg of RNA was used for each cDNA synthesis reaction by Superscript IV (Invitrogen) and random hexamers as per manufacturer's recommendation. The CFX96 touch (Biorad) real time PCR was used for qRT-PCRs. qRT-PCRs were performed using three biological replicates for each sample. The fold changes were calculated by the ΔΔCt method and individual expression data was normalized to pre c-myc. The *p*-values were calculated by Student's unpaired two-tailed *t*-test. qRT-PCR primers are listed in Supplementary Table 1.

X-ray induced Senescence:

BJ fibroblast were cultured in (DMEM) Dulbecco's Modified Eagle's medium supplemented with 10% Fetal Bovine Serum and 1% Penicillin/Streptomycin at 37 °C in a humidified incubator containing 5% CO2. Cells were first immortalized by expressing hTERT. Cells were then seeded at around 40% confluency. The day after seeding, a single dose of 10 Gy was delivered using CIX3 cabinet x-ray irradiator (xstrahl Life Sciences) with (195 kV, 10 mA).The irradiated cells were not passaged, but the medium was changed on Days 4, 8,12 and 16 and cells were either harvested on day 10 or day 20 and used for RNA isolation and Chip experiments respectively. Senescence was confirmed by SA-β-gal staining (Cell Signaling technology #9860) and p21 expression (p21 Santacruz Biotechnology sc-397).

siRNA transfection:

siRNAs SMARTpools for scrambled (cat no D-001810-10-05) and CTCF siRNA (L-020165-00-0005) were purchased from GE Dharmacon. Transfections were done using Lipofectamine 2000 (Invitrogen cat no 11668027).

Antibodies:

Antibodies used were, CTCF (cell signaling, 3418), , DDX5 (abcam, ab-21696), Cdkn2A p16 (abcam, ab-108349), ARF p14 (Santacruz Biotechnology, sc-53639), PolII (Santacruz Biotechnology, sc-55492), GAPDH (Santacruz Biotechnology, sc-32233), Histone H3 (Sigma-Aldrich H0164).

TCGA tumor data analysis:

Cancer specific ATAC-seq peaks for CESC from TCGA cohort were obtained from https://gdc.cancer.gov/. Gene expression for CESC belonging to the TCGA cohort were also obtained from https://gdc.cancer.gov/. TADs and boundaries from HeLa were interrogated in tumor datasets.

ChIP-seq and Cut and Run analysis:

The sequenced reads were aligned to hg19 assembly using default Bowtie2 options. Tag directories were made from the aligned reads using HOMER (http://homer.ucsd.edu/homer/) makeTagDirectory command. A 200bp sliding window was used to identify narrow peaks of transcription factors' ChIP-seq and CTCF Cut and Run which are characteristic of transcription factor peaks. The artifacts from clonal amplification were neglected as only one tag from each unique genomic position was considered (-tbp 1). The threshold was set at a false discovery rate (FDR) of 0.001 determined by peak finding using randomized tag positions in a genome with an effective size of 2 × 10^9 bp. For histone marks, seed regions were initially found using a peak size of 500bp (FDR<0.001) to identify enriched loci. Enriched regions separated by <1kb were merged and considered as blocks of variable lengths. HOMER makeUCSCfile command was used to generate bedgraph files of the read densities across the genome and this track was uploaded to UCSC genome browser. The tag directories generated were used to quantify signal at various regions of interest using annotatePeaks.pl. The datasets used in the study are mentioned in Supplementary Table 3.

GRO-seq analysis:

The sequenced reads were aligned to hg19 assembly using default Bowtie2 options. Tag directories were made from the aligned reads using HOMER makeTagDirectory command. Tag directories were used to quantify signal and quantify gene expression. HOMER makeUCSCfile command was used to generate strand specific bedgraph files of the read densities across the genome and this track was uploaded to UCSC genome browser.

TADs and loop domain calling:

The raw paired reads were trimmed and individually mapped to hg19 assembly using bowtie2. The HOMER program makeTagDirectory was first used to create tag directories with tbp 1 option. Data was further processed by HOMER in order to remove small fragment and self-ligations using makeTagDirectory with the following options: -removePEbg -removeSpikes 10000 5. Next, findTADsAndLoops.pl was used to obtain overlapping TADs (TADs and sub-TADs), produced at a 5kb resolution with 10kb windows. This program was also used to generate two bedGraph files that describe the directionality index and the insulation score. tagDir2hicFile.pl was used to generate .hic files. WashU epigenome browser was used to visualize the HiC data. Boundaries of the TADs were defined as 5kb or 20kb regions centred at the end of the TADs called. HICCUPS was used to obtain loops anchors from the earlier obtained .hic file at a 5kb resolution. HOMER annotatePeaks.pl was used to quantify signal from tagDirectories, count peaks, quantify insulation and annotate features at the TAD boundaries. Non-genic TAD boundaries were identified as those that did NOT intersect with an annotated gene body. GRO-seq signal was used to rank the boundaries to then select 10% unique boundaries in each category (high transcription, low transcription, no transcription and random). The .hic file was converted to .cool. The obtained file was then used to plot the averaged insulation score valleys at 5 kb resolution and 100 kb around the boundary using coolpup.py.

NET-CAGE and CAGE Analysis:

NET-CAGE and CAGE sequenced reads were aligned to hg19 using bowtie2. The HOMER program makeTagDirectory was first used to create tag directories. findPeaks with "–style tss" was used to obtain NET-CAGE TSS. TSS identified within 1kb of each other on the same strand were then merged. The NET-CAGE identified TSS intersecting the refseq annotated TSS was called mRNA TSS and the rest were defined as eRNA TSS. Those TSS which fall in boundaries were identified as bmRNA or beRNAs. 2kb around the identified TSS was used to quantify NET-CAGE and CAGE signal to calculate the log2 fold change between the two.

5' Splice site and Transcription Termination Site Sequence Analysis:

To identify the 5' SS motif, HOMER denovo motif analysis was performed on the 500bp region after the Refseq annotated TSS with other H3K27ac 500bp regions as background. The top hit was observed to be the splice acceptor site. The "AATAAA" motif was used as the terminator polyA sequence. HOMER scanMotifGenomeWide was used to identify "predicted" splice sites and polyA terminator sites using the earlier identified motifs. The occurrence of the predicted sites was plotted at the earlier identified TSS.

Circular Chromatin Conformation Capture-seq:

4C was performed as per the protocol described in van de Werken et al., 2012 with minor variations. HeLa cells were fixed with fresh formaldehyde (1.5%) and quenched with glycine (125mM) followed by washes with ice-cold PBS (2x) and scraped, pelleted and stored at -80^{0}C. Lysis buffer [Tris-Cl pH 8.0 (10mM), NaCl (10mM), NP-40 (0.2%), PIC (1x)] was added to the pellets and homogenized by Dounce homogenizer (20 stroked with pestle A followed by pestle B). The 3C digestion was performed with HindIII (400units, NEB) and ligation was performed by the T4 DNA ligase and ligation mix [Triton X-100 (1%), Ligation buffer (1x), BSA (0.105mg/ml), ATP (1.05mM)]. 10x Ligation buffer- Tris-Cl pH 7.5 (500mM), MgCl2 (100mM), DTT (100mM). The ligated samples were then purified by PCI purification and subjected to ethanol precipitation and the pellet was eluted in TE (pH 8.0) to obtain the 3C library. The 4C digestion was performed by DpnII (50units, NEB) and the samples were ligated, purified and precipitated similar to the 3C library to obtain the 4C library. The 4C library was subjected to RNaseA treatment and purified

by the QIAquick PCR purification kit. The concentration of the library was then measured by Nanodrop and subjected to PCRs using the oligos for the enhancer viewpoint. The samples were next PCR purified using the same kit and subjected to next-generation sequencing with Illumina HiSeq2500 using 50bp single-end reads. The 4C data is mentioned in Supplementary Table 2.

4C method and analysis:

The sequenced reads were aligned to hg19 assembly as described in R.4Cker (https://github.com/rr1859/R.4Cker) with Bowtie2. Data analysis was further performed using 4C-ker with default parameters. 4Cseqpipe (http://compgenomics.weizmann.ac.il/tanay/?page_id=367) was also used to process the sequenced data. 4C-seq images were generated using truncated mean at a 10kb resolution.

Motif analysis:

annotatePeaks.pl was used with –hist option with the CTCF motif probability matrix to plot the motif occurrence in the peaks.

Promoter capture analysis:

Processed CHiCAGO data from Thiecke et al. (https://osf.io/brzuc/) was obtained. BEDTools suite was used to obtain interactions of interest and perform further analysis. The promoter interacting region of the Bedpe files of pcHiC interactions were then intersected with boundaries to obtain promoters that interact with boundaries. The strength of the interactions obtained from the processed CHiCAGO data was plotted for interactions from boundary interacting promoters to enhancers (H3K27ac regions).

RNA-seq analysis:

The raw reads were mapped to hg19 assembly using hisat2 in a strand specific manner. Tag directories were made from the aligned reads using HOMER makeTagDirectory command.

HOMER makeUCSCfile command was used to generate strand specific bedgraph files of the read densities across the genome and this track was uploaded to UCSC genome browser.

References:

Andersson, R., Gebhard, C., Miguel-Escalada, I. et al. An atlas of active enhancers across human cell types and tissues. Nature 507, 455–461 (2014). https://doi.org/10.1038/nature12787

Arzate-Mejía RG, Josué Cerecedo-Castillo A, Guerrero G, Furlan-Magaril M, Recillas-Targa F. 2020. In situ dissection of domain boundaries affect genome topology and gene transcription in Drosophila. *Nat Commun*. doi:10.1038/s41467-020-14651-z

Barutcu AR, Blencowe BJ, Rinn JL. 2019. Differential contribution of steady-state RNA and active transcription in chromatin organization . *EMBO Rep*. doi:10.15252/embr.201948068

Bonev B, Mendelson Cohen N, Szabo Q, Fritsch L, Papadopoulos GL, Lubling Y, Xu X, Lv X, Hugnot JP, Tanay A, Cavalli G. 2017. Multiscale 3D Genome Rewiring during Mouse Neural Development. *Cell*. doi:10.1016/j.cell.2017.09.043

Bouvy-Liivrand M, De Sande AH, Pölönen P, Mehtonen J, Vuorenmaa T, Niskanen H, Sinkkonen L, Kaikkonen MU, Heinäniemi M. 2017. Analysis of primary microRNA loci from nascent transcriptomes reveals regulatory domains governed by chromatin architecture. *Nucleic Acids Res*. doi:10.1093/nar/gkx680

Dekker J, Mirny L. 2016. The 3D Genome as Moderator of Chromosomal Communication. *Cell*. doi:10.1016/j.cell.2016.02.007

Despang A, Schöpflin R, Franke M, Ali S, Jerković I, Paliou C, Chan WL, Timmermann B, Wittler L, Vingron M, Mundlos S, Ibrahim DM. 2019. Functional dissection of the Sox9–Kcnj2 locus identifies nonessential and instructive roles of TAD architecture. *Nat Genet*. doi:10.1038/s41588-019-0466-z

Dixon JR, Selvaraj S, Yue F, Kim A, Li Y, Shen Y, Hu M, Liu JS, Ren B. 2012. Topological domains in mammalian genomes identified by analysis of chromatin interactions. *Nature*. doi:10.1038/nature11082

Farooq U, Saravanan B, Islam Z, Walavalkar K, Singh AK, Jayani RS, Meel S, Swaminathan S, Notani D. An interdependent network of functional enhancers regulates transcription and EZH2 loading at the INK4a/ARF locus. *Cell Rep*. doi: 10.1016/j.celrep.2021.108898.

Flavahan WA, Drier Y, Liau BB, Gillespie SM, Venteicher AS, Stemmer-Rachamimov AO, Suvà ML, Bernstein BE. 2016. Insulator dysfunction and oncogene activation in IDH mutant gliomas. *Nature*. doi:10.1038/nature16490

Fudenberg G, Imakaev M, Lu C, Goloborodko A, Abdennur N, Mirny LA. 2016. Formation of Chromosomal Domains by Loop Extrusion. *Cell Rep*. doi:10.1016/j.celrep.2016.04.085

Gagnon KT, Li L, Janowski BA, Corey DR. 2014. Analysis of nuclear RNA interference in human cells by subcellular fractionation and Argonaute loading. *Nat Protoc*. doi:10.1038/nprot.2014.135

Giorgetti L, Lajoie BR, Carter AC, Attia M, Zhan Y, Xu J, Chen CJ, Kaplan N, Chang HY, Heard E, Dekker J. 2016. Structural organization of the inactive X chromosome in the mouse. *Nature*. doi:10.1038/nature18589

Gong Y, Lazaris C, Sakellaropoulos T, Lozano A, Kambadur P, Ntziachristos P, Aifantis I, Tsirigos A. 2018. Stratification of TAD boundaries reveals preferential insulation of super-enhancers by strong boundaries. *Nat Commun*. doi:10.1038/s41467-018-03017-1

Hansen AS. 2020. CTCF as a boundary factor for cohesin-mediated loop extrusion: evidence for a multi-step mechanism. *Nucleus*. doi:10.1080/19491034.2020.1782024

Hansen AS, Hsieh THS, Cattoglio C, Pustova I, Saldaña-Meyer R, Reinberg D, Darzacq X, Tjian

R. 2019. Distinct Classes of Chromatin Loops Revealed by Deletion of an RNA-Binding Region in CTCF. *Mol Cell*. doi:10.1016/j.molcel.2019.07.039

Hanssen LLP, Kassouf MT, Oudelaar AM, Biggs D, Preece C, Downes DJ, Gosden M, Sharpe JA, Sloane-Stanley JA, Hughes JR, Davies B, Higgs DR. 2017. Tissue-specific CTCF-cohesin-mediated chromatin architecture delimits enhancer interactions and function in vivo. *Nat Cell Biol*. doi:10.1038/ncb3573

Harismendy O, Notani D, Song X, Rahim NG, Tanasa B, Heintzman N, Ren B, Fu XD, Topol EJ, Rosenfeld MG, Frazer KA. 2011. 9p21 DNA variants associated with coronary artery disease impair interferon-γ 3 signalling response. *Nature*. doi:10.1038/nature09753

Hsieh THS, Cattoglio C, Slobodyanyuk E, Hansen AS, Rando OJ, Tjian R, Darzacq X. 2020. Resolving the 3D Landscape of Transcription-Linked Mammalian Chromatin Folding. *Mol Cell*. doi:10.1016/j.molcel.2020.03.002

Hug CB, Grimaldi AG, Kruse K, Vaquerizas JM. 2017. Chromatin Architecture Emerges during Zygotic Genome Activation Independent of Transcription. *Cell*. doi:10.1016/j.cell.2017.03.024

Jayani RS, Singh A, Notani D. 2017. Isolation of nuclear RNA-associated protein complexesMethods in Molecular Biology. doi:10.1007/978-1-4939-6716-2_9

Kentepozidou E, Aitken SJ, Feig C, Stefflova K, Ibarra-Soria X, Odom DT, Roller M, Flicek P. 2020. Clustered CTCF binding is an evolutionary mechanism to maintain topologically associating domains. *Genome Biol*. doi:10.1186/s13059-019-1894-x

Khoury A, Achinger-Kawecka J, Bert SA, Smith GC, French HJ, Luu PL, Peters TJ, Du Q, Parry AJ, Valdes-Mora F, Taberlay PC, Stirzaker C, Statham AL, Clark SJ. 2020. Constitutively bound CTCF sites maintain 3D chromatin architecture and long-range epigenetically regulated domains. *Nat Commun*. doi:10.1038/s41467-019-13753-7

Kloetgen A, Thandapani P, Ntziachristos P, Ghebrechristos Y, Nomikou S, Lazaris C, Chen X, Hu H, Bakogianni S, Wang J, Fu Y, Boccalatte F, Zhong H, Paietta E, Trimarchi T, Zhu Y, Van Vlierberghe P, Inghirami GG, Lionnet T, Aifantis I, Tsirigos A. 2020. Three-dimensional chromatin landscapes in T cell acute lymphoblastic leukemia. *Nat Genet*. doi:10.1038/s41588-020-0602-9

Krivega I, Dean A. 2017. CTCF fences make good neighbours. *Nat Cell Biol*. doi:10.1038/ncb3584

Li W, Notani D, Ma Q, Tanasa B, Nunez E, Chen AY, Merkurjev D, Zhang J, Ohgi K, Song X, Oh S, Kim HS, Glass CK, Rosenfeld MG. 2013. Functional roles of enhancer RNAs for oestrogen-dependent transcriptional activation. *Nature*. doi:10.1038/nature12210

Li W, Notani D, Rosenfeld MG. 2016. Enhancers as non-coding RNA transcription units: Recent insights and future perspectives. *Nat Rev Genet*. doi:10.1038/nrg.2016.4

Matthews BJ, Waxman DJ. Computational prediction of CTCF/cohesin-based intra-TAD loops that insulate chromatin contacts and gene expression in mouse liver. Elife. 2018 May 14;7:e34077. doi: 10.7554/eLife.34077

McLaughlin-Drubin ME, Park D, Munger K. Tumor suppressor p16INK4A is necessary for survival of cervical carcinoma cell lines. Proc Natl Acad Sci U S A. 2013;110(40):16175-16180. doi:10.1073/pnas.1310432110

Nakahashi H, Kwon KRK, Resch W, Vian L, Dose M, Stavreva D, Hakim O, Pruett N, Nelson S, Yamane A, Qian J, Dubois W, Welsh S, Phair RD, Pugh BF, Lobanenkov V, Hager GL, Casellas R. 2013. A Genome-wide Map of CTCF Multivalency Redefines the CTCF Code. *Cell Rep*. doi:10.1016/j.celrep.2013.04.024

NandyMazumdar M, Yin S, Paranjapye A, Kerschner JL, Swahn H, Ge A, Leir SH, Harris A. 2020. Looping of upstream cis-regulatory elements is required for CFTR expression in human airway epithelial cells. *Nucleic Acids Res*. doi:10.1093/nar/gkaa089

Narendra V, Rocha PP, An D, Raviram R, Skok JA, Mazzoni EO, Reinberg D. 2015. CTCF establishes discrete functional chromatin domains at the Hox clusters during differentiation. *Science (80-)*. doi:10.1126/science.1262088

Nilson KA, Lawson CK, Mullen NJ, Ball CB, Spector BM, Meier JL, Price DH. 2017. Oxidative stress rapidly stabilizes promoter-proximal paused Pol II across the human genome. *Nucleic Acids Res*. doi:10.1093/nar/gkx724

Nora EP, Goloborodko A, Valton AL, Gibcus JH, Uebersohn A, Abdennur N, Dekker J, Mirny LA, Bruneau BG. 2017. Targeted Degradation of CTCF Decouples Local Insulation of Chromosome Domains from Genomic Compartmentalization. *Cell*. doi:10.1016/j.cell.2017.05.004

Nuebler J, Fudenberg G, Imakaev M, Abdennur N, Mirny LA. 2018. Chromatin organization by an interplay of loop extrusion and compartmental segregation. *Proc Natl Acad Sci U S A*. doi:10.1073/pnas.1717730115

Pauck A, Lener B, Hoell M, Kaiser A, Kaufmann AM, Zwerschke W, Jansen-Dürr P. Depletion of the cdk inhibitor p16INK4a differentially affects proliferation of established cervical carcinoma cells. J Virol. 2014 May;88(10):5256-62. doi: 10.1128/JVI.03817-13.

Pugacheva EM, Kubo N, Loukinov D, Tajmul M, Kang S, Kovalchuk AL, Strunnikov A V., Zentner GE, Ren B, Lobanenkov V V. 2020. CTCF mediates chromatin looping via N-terminal domain-dependent cohesin retention. *Proc Natl Acad Sci U S A*. doi:10.1073/pnas.1911708117

Rahnamoun H, Lee J, Sun Z, Lu H, Ramsey KM, Komives EA, Lauberth SM. 2018. RNAs interact with BRD4 to promote enhanced chromatin engagement and transcription activation. *Nat Struct Mol Biol*. doi:10.1038/s41594-018-0102-0

Rao SSP, Huang SC, Glenn St Hilaire B, et al. Cohesin loss eliminates all loop domains. *Cell*. 2017;171(2):305–320.e24.

Rao SSP, Huntley MH, Durand NC, Stamenova EK, Bochkov ID, Robinson JT, Sanborn AL, Machol I, Omer AD, Lander ES, Aiden EL. 2014. A 3D map of the human genome at kilobase resolution reveals principles of chromatin looping. *Cell*. doi:10.1016/j.cell.2014.11.021

Rowley MJ, Nichols MH, Lyu X, Ando-Kuri M, Rivera ISM, Hermetz K, Wang P, Ruan Y, Corces VG. 2017. Evolutionarily Conserved Principles Predict 3D Chromatin Organization. *Mol Cell*. doi:10.1016/j.molcel.2017.07.022

Saldaña-Meyer R, Rodriguez-Hernaez J, Escobar T, Nishana M, Jácome-López K, Nora EP, Bruneau BG, Tsirigos A, Furlan-Magaril M, Skok J, Reinberg D. 2019. RNA Interactions Are Essential for CTCF-Mediated Genome Organization. *Mol Cell*. doi:10.1016/j.molcel.2019.08.015

Schlackow M, Nojima T, Gomes T, Dhir A, Carmo-Fonseca M, Proudfoot NJ. 2017. Distinctive Patterns of Transcription and RNA Processing for Human lincRNAs. *Mol Cell*. doi:10.1016/j.molcel.2016.11.029

Schwarzer W, Abdennur N, Goloborodko A, et al. Two independent modes of chromatin organization revealed by cohesin removal. *Nature*. 2017;551(7678):51–56

Skene PJ, Henikoff S. An efficient targeted nuclease strategy for high-resolution mapping of DNA binding sites. Elife. 2017 Jan 16;6:e21856. doi: 10.7554/eLife.21856

Sima J, Chakraborty A, Dileep V, Michalski M, Klein KN, Holcomb NP, Turner JL, Paulsen MT, Rivera-Mulia JC, Trevilla-Garcia C, Bartlett DA, Zhao PA, Washburn BK, Nora EP, Kraft K, Mundlos S, Bruneau BG, Ljungman M, Fraser P, Ay F, Gilbert DM. 2019. Identifying cis Elements for Spatiotemporal Control of Mammalian DNA Replication. *Cell*. doi:10.1016/j.cell.2018.11.036

Sun F, Chronis C, Kronenberg M, Chen XF, Su T, Lay FD, Plath K, Kurdistani SK, Carey MF. 2019. Promoter-Enhancer Communication Occurs Primarily within Insulated Neighborhoods. *Mol Cell*. doi:10.1016/j.molcel.2018.10.039

Szabo Q, Donjon A, Jerković I, Papadopoulos GL, Cheutin T, Bonev B, Nora EP, Bruneau BG, Bantignies F, Cavalli G. 2020. Regulation of single-cell genome organization into TADs and chromatin nanodomains. *Nat Genet*. doi:10.1038/s41588-020-00716-8

Thakur J, Fang H, Llagas T, Disteche CM, Henikoff S. Architectural RNA is required for heterochromatin organization. doi: https://doi.org/10.1101/784835

Thiecke MJ, Wutz G, Muhar M, Tang W, Bevan S, Malysheva V, Stocsits R, Neumann T, Zuber J, Fraser P, Schoenfelder S, Peters JM, Spivakov M. 2020. Cohesin-Dependent and -Independent Mechanisms Mediate Chromosomal Contacts between Promoters and Enhancers. *Cell Rep*. doi:10.1016/j.celrep.2020.107929

Williamson I, Kane L, Devenney PS, Flyamer IM, Anderson E, Kilanowski F, Hill RE, Bickmore WA, Lettice LA. 2019. Developmentally regulated Shh expression is robust to TAD perturbations. *Dev*. doi:10.1242/dev.179523

Wutz G, Várnai C, Nagasaka K, et al. Topologically associating domains and chromatin loops depend on cohesin and are regulated by CTCF, WAPL, and PDS5 proteins. *Embo J*. 2017;36(24):3573–3599

Yang M, Vesterlund M, Siavelis I, Moura-Castro LH, Castor A, Fioretos T, Jafari R, Lilljebjörn H, Odom DT, Olsson L, Ravi N, Woodward EL, Harewood L, Lehtiö J, Paulsson K. 2019. Proteogenomics and Hi-C reveal transcriptional dysregulation in high hyperdiploid childhood acute lymphoblastic leukemia. *Nat Commun*. doi:10.1038/s41467-019-09469-3

Yokoshi M, Segawa K, Fukaya T. 2020. Visualizing the Role of Boundary Elements in Enhancer-Promoter Communication. *Mol Cell*. doi:10.1016/j.molcel.2020.02.007

Zhang D, Huang P, Sharma M, Keller CA, Giardine B, Zhang H, Gilgenast TG, Phillips-Cremins JE, Hardison RC, Blobel GA. 2020. Alteration of genome folding via contact domain boundary insertion. *Nat Genet*. doi:10.1038/s41588-020-0680-8

Zhang J, Lee D, Dhiman V, Jiang P, Xu Jie, McGillivray P, Yang H, Liu J, Meyerson W, Clarke D, Gu M, Li S, Lou S, Xu Jinrui, Lochovsky L, Ung M, Ma L, Yu S, Cao Q, Harmanci A, Yan KK, Sethi A, Gürsoy G, Schoenberg MR, Rozowsky J, Warrell J, Emani P, Yang YT, Galeev T, Kong X, Liu S, Li X, Krishnan J, Feng Y, Rivera-Mulia JC, Adrian J, Broach JR, Bolt M, Moran J, Fitzgerald D, Dileep V, Liu T, Mei S, Sasaki T, Trevilla-Garcia C, Wang S, Wang Y, Zang C, Wang D, Klein RJ, Snyder M, Gilbert DM, Yip K, Cheng C, Yue F, Liu XS, White KP, Gerstein M. 2020. An integrative ENCODE resource for cancer genomics. *Nat Commun*. doi:10.1038/s41467-020-14743-w

Zhang Y, Li T, Preissl S, Amaral ML, Grinstein JD, Farah EN, Destici E, Qiu Y, Hu R, Lee AY, Chee S, Ma K, Ye Z, Zhu Q, Huang H, Fang R, Yu L, Izpisua Belmonte JC, Wu J, Evans SM, Chi NC, Ren B. 2019. Transcriptionally active HERV-H retrotransposons demarcate topologically associating domains in human pluripotent stem cells. *Nat Genet*. doi:10.1038/s41588-019-0479-7

Zirkel A, Nikolic M, Sofiadis K, Mallm JP, Brackley CA, Gothe H, Drechsel O, Becker C,

Altmüller J, Josipovic N, Georgomanolis T, Brant L, Franzen J, Koker M, Gusmao EG, Costa IG, Ullrich RT, Wagner W, Roukos V, Nürnberg P, Marenduzzo D, Rippe K, Papantonis A. 2018. HMGB2 Loss upon Senescence Entry Disrupts Genomic Organization and Induces CTCF Clustering across Cell Types. *Mol Cell*. doi:10.1016/j.molcel.2018.03.030

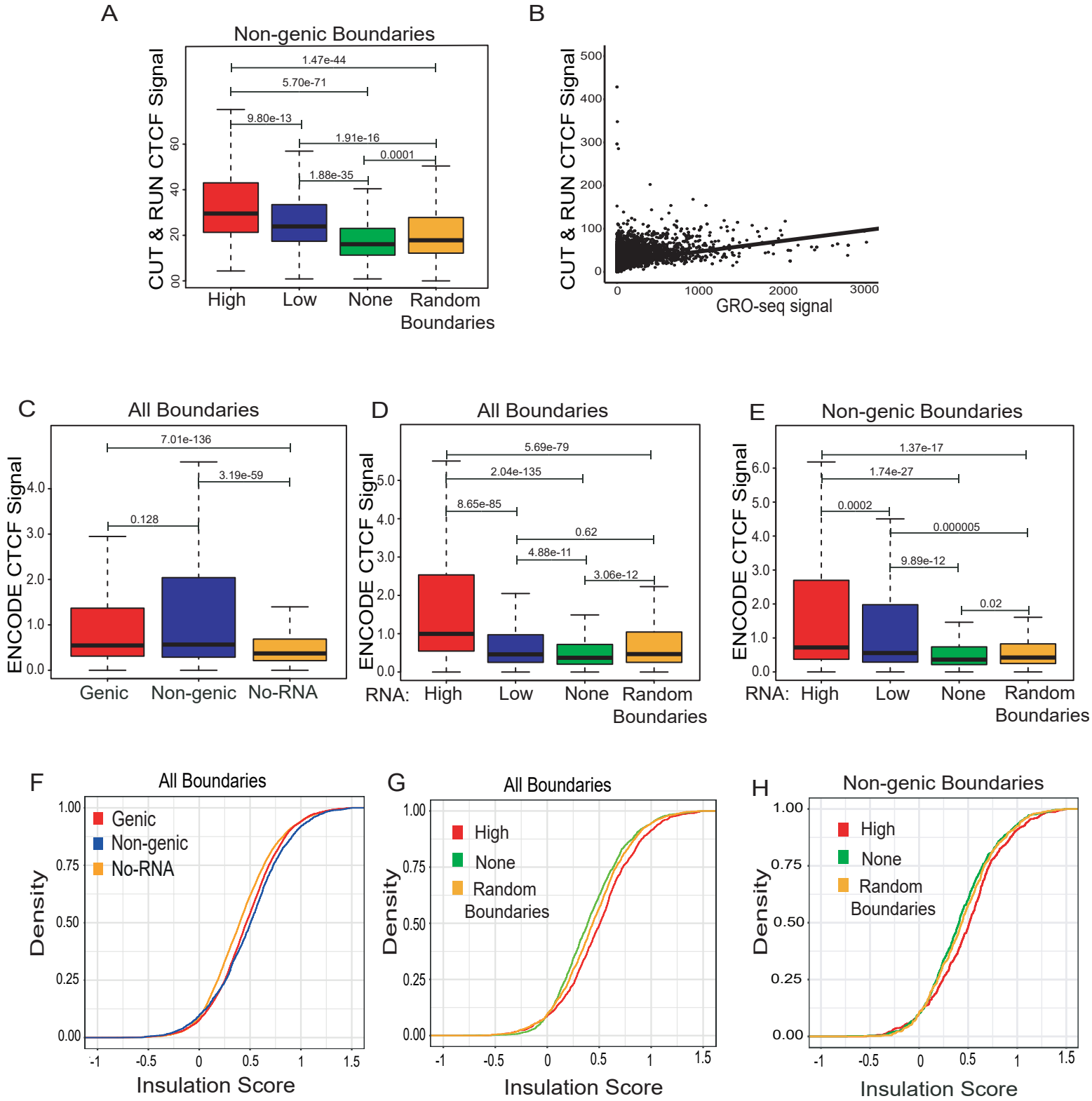

Islam and Saravanan et al Sup Fig. 1

Supp Figure 1. Transcribing boundaries exhibit better insulation: A. CTCF enrichment (CTCF cut & run) on non-genic transcribing boundaries with high, low bRNA vs. non-transcribing and random boundaries **B.** levels of bRNA and CTCF occupancy at the TAD boundaries have direct positive correlation. **C.** CTCF enrichment (ChIP-seq) on transcribing genic, non-genic and non-transcribing boundaries. **D.** CTCF enrichment on all transcribing boundaries with high, low bRNA vs. non-transcribing and random boundaries. **E.** CTCF enrichment on non-genic transcribing boundaries with high, low bRNA vs. non-transcribing and random boundaries. **F.** Density plot showing insulation score of transcribing genic, non-genic and non-transcribing boundaries **G.** Density plot showing insulation score of all transcribing boundaries exhibiting varying levels of bRNA vs. non-transcribing and random boundaries **H.** Density plot showing insulation score of non-genic transcribing boundaries exhibiting varying levels of bRNA vs. non-transcribing and random boundaries. p-values in boxplots were calculated by Mann Whitney test (Wilcoxon two-sided rank sum test). The boxplots depict the minimum (Q1-1.5*IQR), first quartile, median, third quartile and maximum (Q3+1.5*IQR) without outliers.

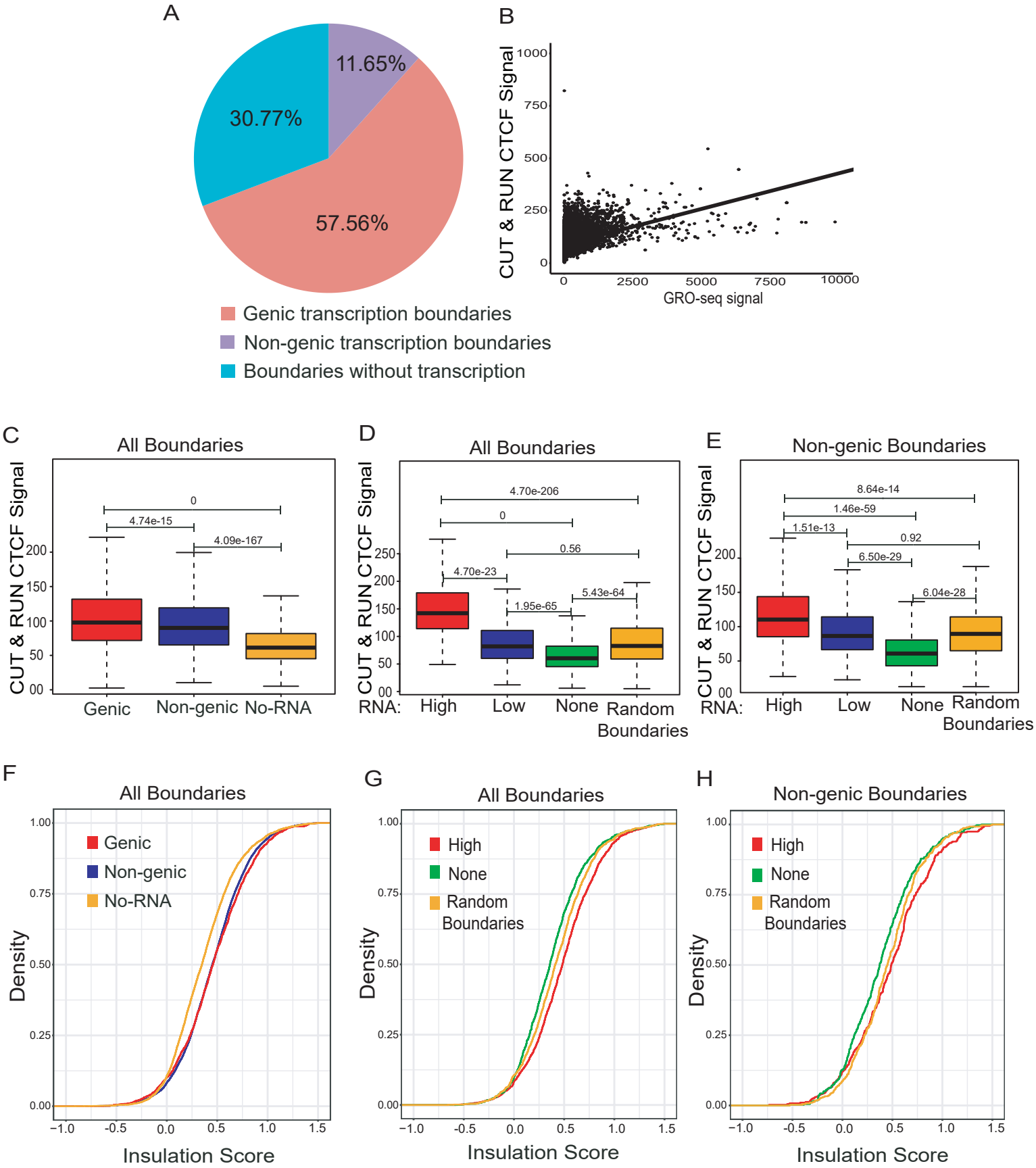

Islam and Saravanan et al Sup Fig. 2

Supp Figure 2. boundaries defined by 20 kb resolution show the similar features as 5kb resolution:

A. Pie diagram showing the percentage of boundaries that show genic, non-genic transcription and not transcribing boundaries. **B.** levels of bRNA and CTCF occupancy at the TAD boundaries have direct positive correlation. **C.** CTCF enrichment on transcribing genic, non-genic and non-transcribing boundaries. **D.** CTCF enrichment on all transcribing boundaries with high, low bRNA vs. non-transcribing and random boundaries. **E.** CTCF enrichment on non-genic transcribing boundaries with high, low bRNA vs. non-transcribing and random boundaries. **F.** Density plot showing insulation score of transcribing genic, non-genic and non-transcribing boundaries. **G.** Density plot showing insulation score of all transcribing boundaries exhibiting varying levels of bRNA vs. non-transcribing and random boundaries. **H** Density plot showing insulation score of non-genic transcribing boundaries exhibiting varying levels of bRNA vs. non-transcribing and random boundaries. p-values in boxplots were calculated by Mann Whitney test (Wilcoxon two-sided rank sum test). The boxplots depict the minimum (Q1-1.5*IQR), first quartile, median, third quartile and maximum (Q3+1.5*IQR) without outliers.

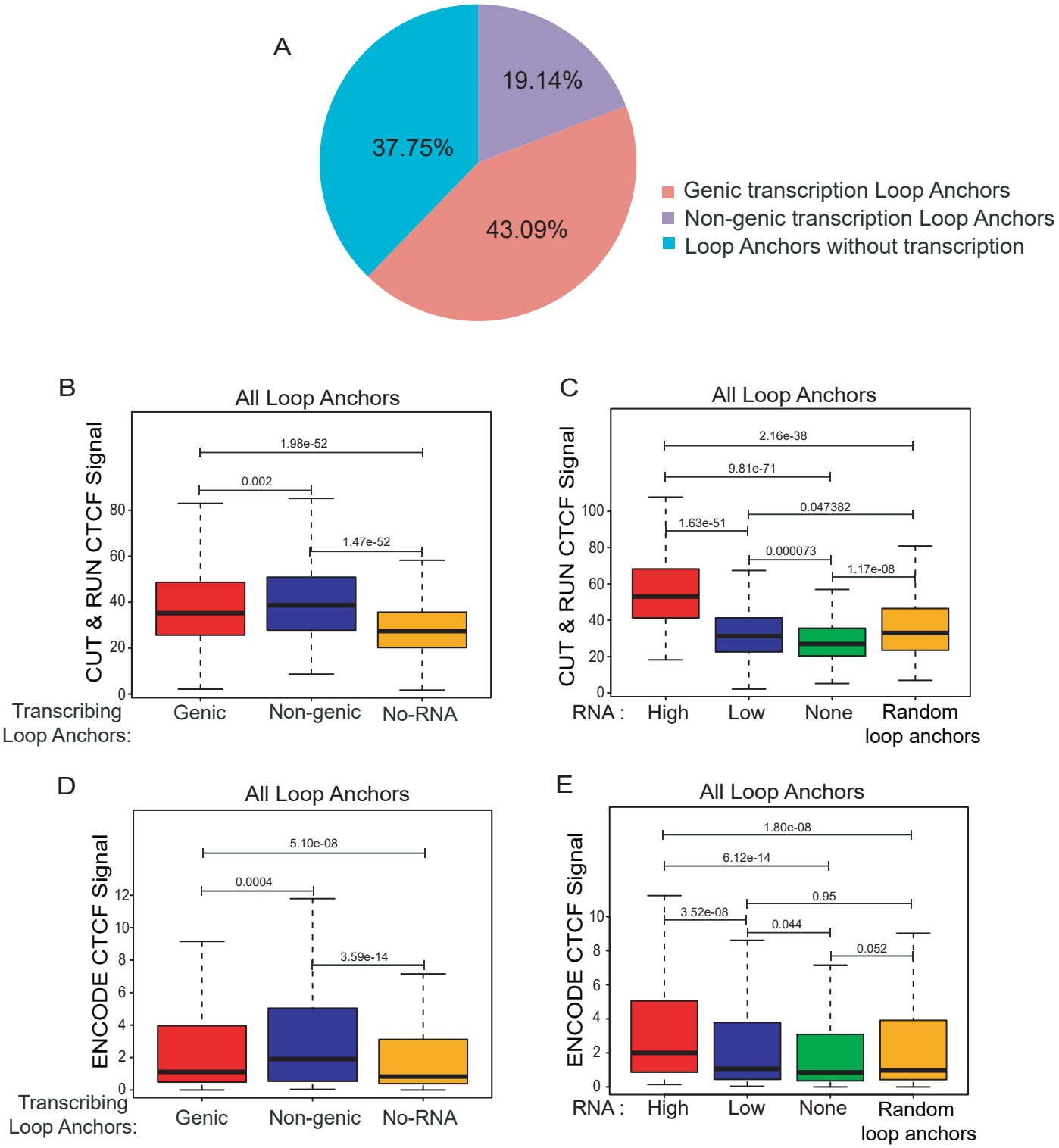

Islam and Saravanan et al Sup Fig. 3

Supp Figure 3. Transcribing Loop Anchors exhibit more CTCF enrichment: A. Pie diagram showing the percentage of loop anchors that overlap with genic transcription, non-genic de novo transcription and without transcription. **B.** CTCF enrichment (CTCF cut & run) on transcribing genic, non-genic and non-transcribing loop anchors. **C.** CTCF enrichment on all transcribing loop anchors with high, low bRNA vs. non-transcribing and random loop anchors. **D.** CTCF enrichment (CTCF ChIP-seq) on transcribing genic, non-genic and non-transcribing loop anchors. **E.** CTCF enrichment on all transcribing loop anchors with high, low bRNA vs. non-transcribing and random loop anchors. p-values in boxplots were calculated by Mann Whitney test (Wilcoxon two-sided rank sum test). The boxplots depict the minimum (Q1-1.5*IQR), first quartile, median, third quartile and maximum (Q3+1.5*IQR) without outliers.

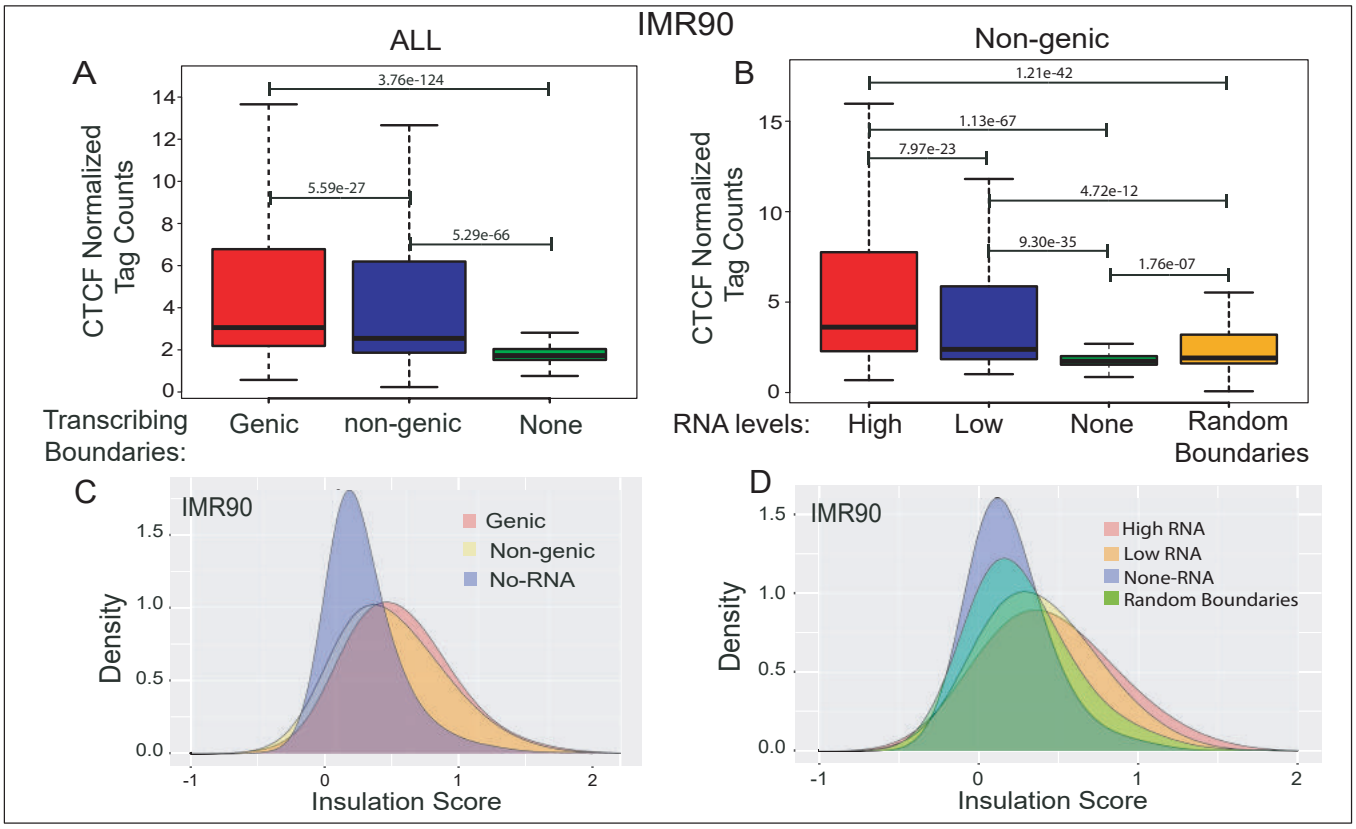

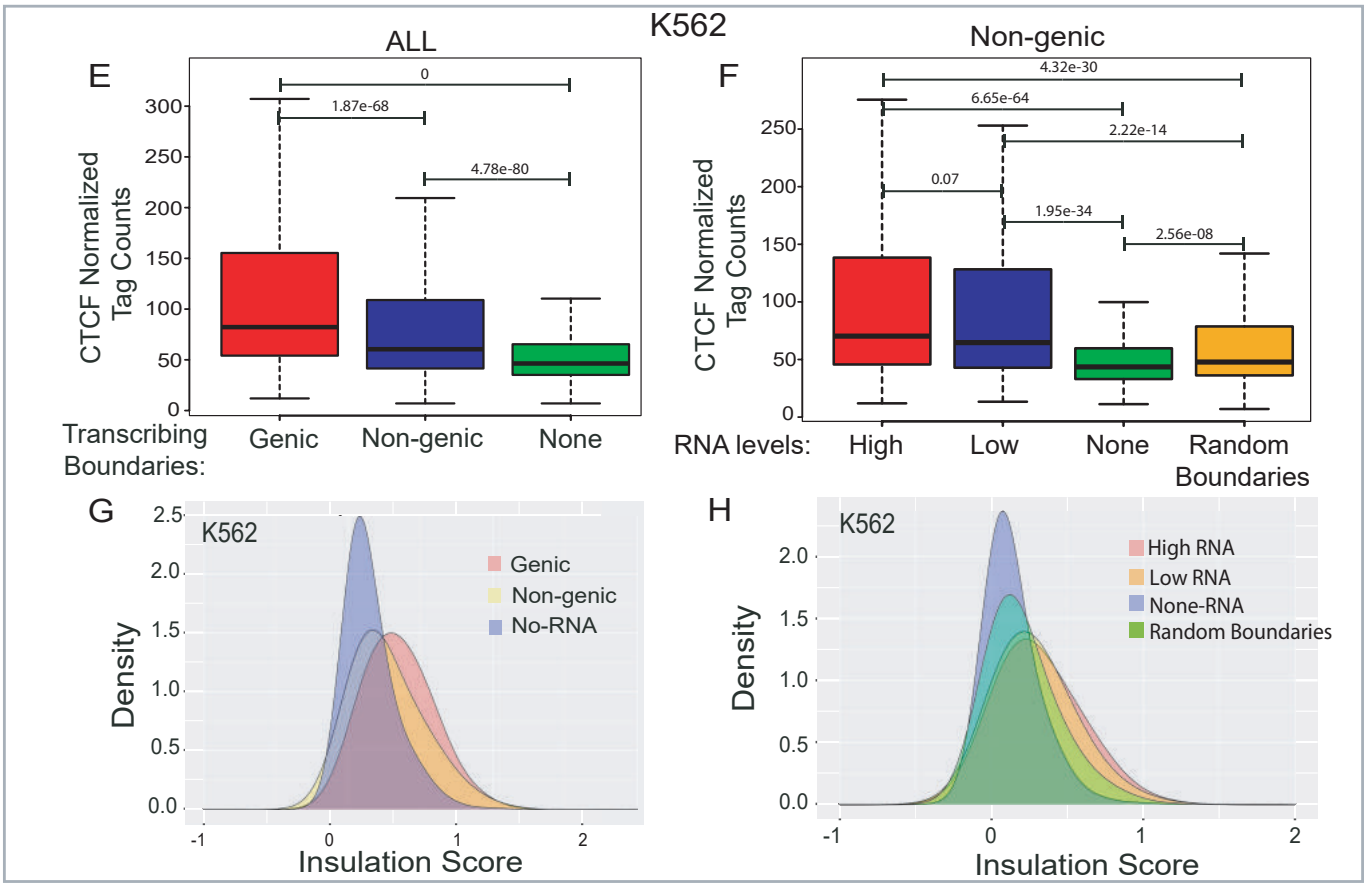

Islam and Saravanan et al Sup Fig. 4

Supp Figure 4. Transcribing boundaries in IMR90 and K562 also exhibit better insulation: **A.** CTCF enrichment on transcribing genic, non-genic and non-transcribing boundaries in IMR90. **B.** CTCF enrichment on non-genic transcribing boundaries with high, low bRNA vs. non-transcribing and random boundaries in IMR90. **C.** Density plots showing insulation score of transcribing genic, non-genic and non-transcribing boundaries in IMR90**. D.** Density plots showing insulation score of non-genic transcribing boundaries exhibiting varying levels of bRNA vs. non-transcribing and random boundaries in IMR90. **E-F**. Plots similar to A-B in K562. **G-H.** Plots similar to C-D in K562. p-values in boxplots were calculated by Mann Whitney test (Wilcoxon two-sided rank sum test). The boxplots depict the minimum (Q1-1.5*IQR), first quartile, median, third quartile and maximum (Q3+1.5*IQR) without outliers.

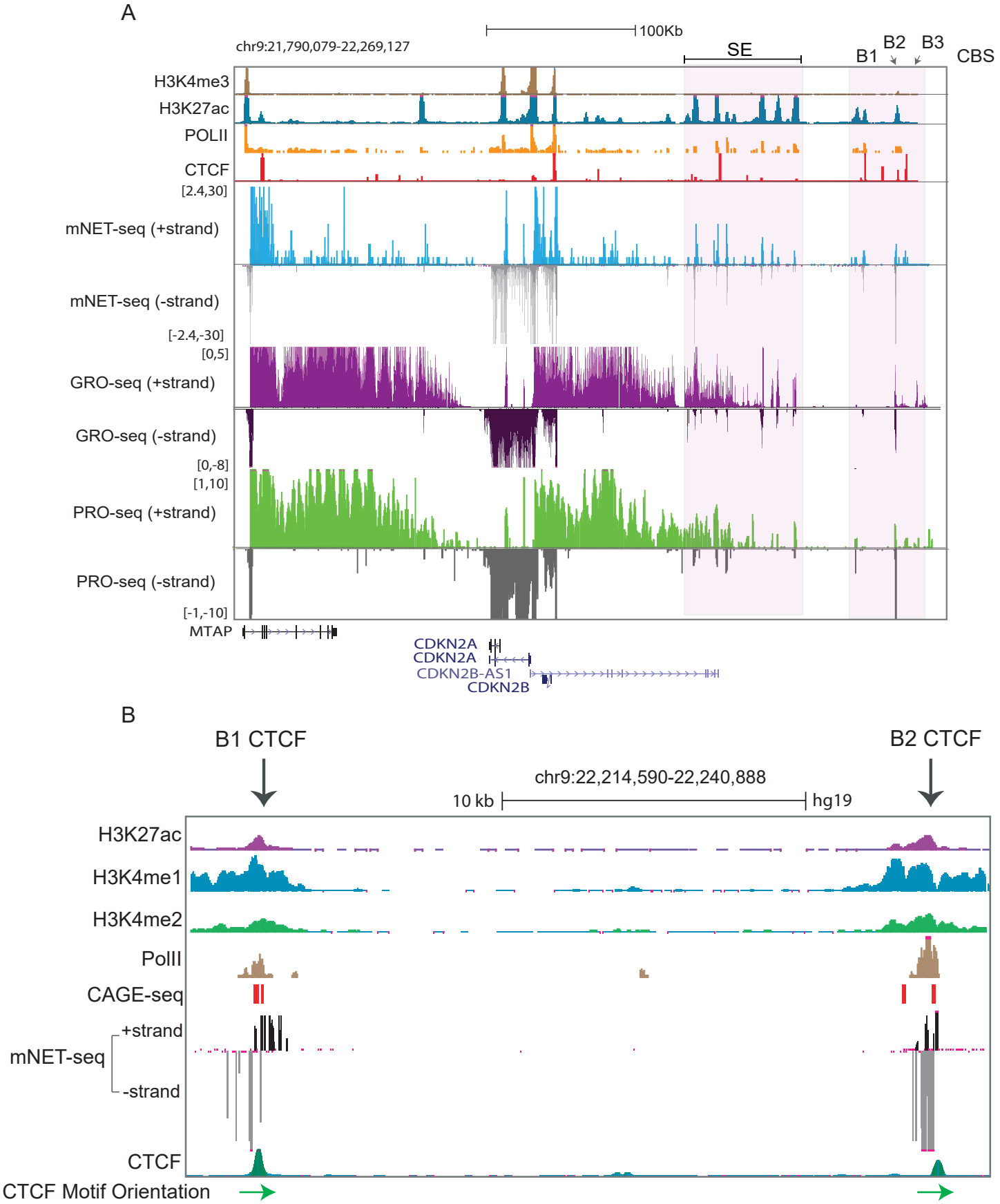

Islam and Saravanan et al. Supp Figure 5

Supp Figure 5. Browser shots of INK4a/ARF loop domain: A. The browser shot showing INK4a/ARF locus on 9p21 region. This is overlaid by the position of, H3K4me3, H3K27ac (enhancers), PolII, CTCF, mNET-seq tracks, GRO seq tracks, PRO seq tracks and gene annotations. The highlighted region shows the B1, B2 and B3 CTCF sites on 3' boundary, and super enhancer. **B**. The browser shot showing the zoomed in region of 3' boundary (B1 and B2 CTCF sites). Which is overlaid by the position of, H3K27ac, H3K4me1, H3K4me2, PolII, CAGE seq track, mNET-seq tracks and CTCF peaks. The Arrow heads at the bottom show CTCF motif orientation at the B1 and B2 CTCF sites .

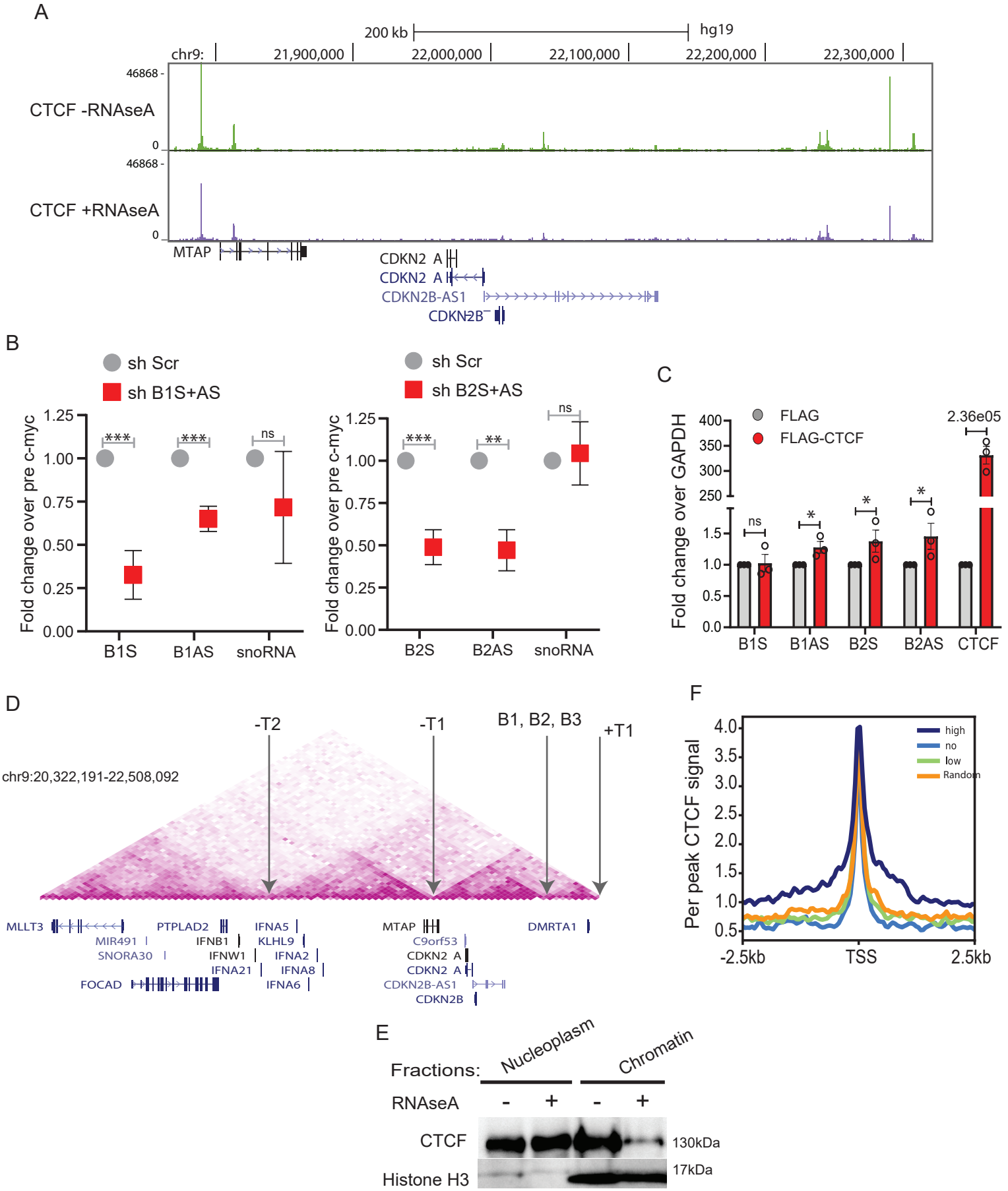

Islam and Saravanan et al. Supp Figure 6

Supp Figure 6. RNA augment the recruitment of CTCF at the TAD boundary: A. The browser shot showing the CTCF cut and run peaks at INK4a/ARF TAD with and without RNaseA treatment. **B.** qRT-PCRs showing the levels of; sense and anti-sense non-coding RNA at B1and B2 CTCF sites and of snoRNA upon B1 and B2 RNA knockdown in chromatin associated RNA fraction**. C.** qRT-PCRs showing the fold change in sense and anti-sense RNAs from B1 and B2 CTCF sites upon Flag-CTCF over expression. Last two bars show the increase in CTCF levels. **D.** TADs around INK4a/ARF TAD and position of arrows shows the CTCF sites at upstream and downstream TAD boundaries where CTCF occupancy was interrogated. **E.** Immunoblotting with CTCF and Histone H3 on soluble nucleoplasm and chromatin bound fractions of the nucleus treated with or without RNaseA **F.** CTCF cut & Run signal at CTCF sites within different categories of boundaries. Error bars denote SEM from three biological replicates. *p*-values were calculated by Student's two-tailed unpaired *t*-test in **B** and **C.** ****$p < 0.0001$,****$p < 0.0001$,*$p < 0.05$, $^{ns}p > 0.05$.

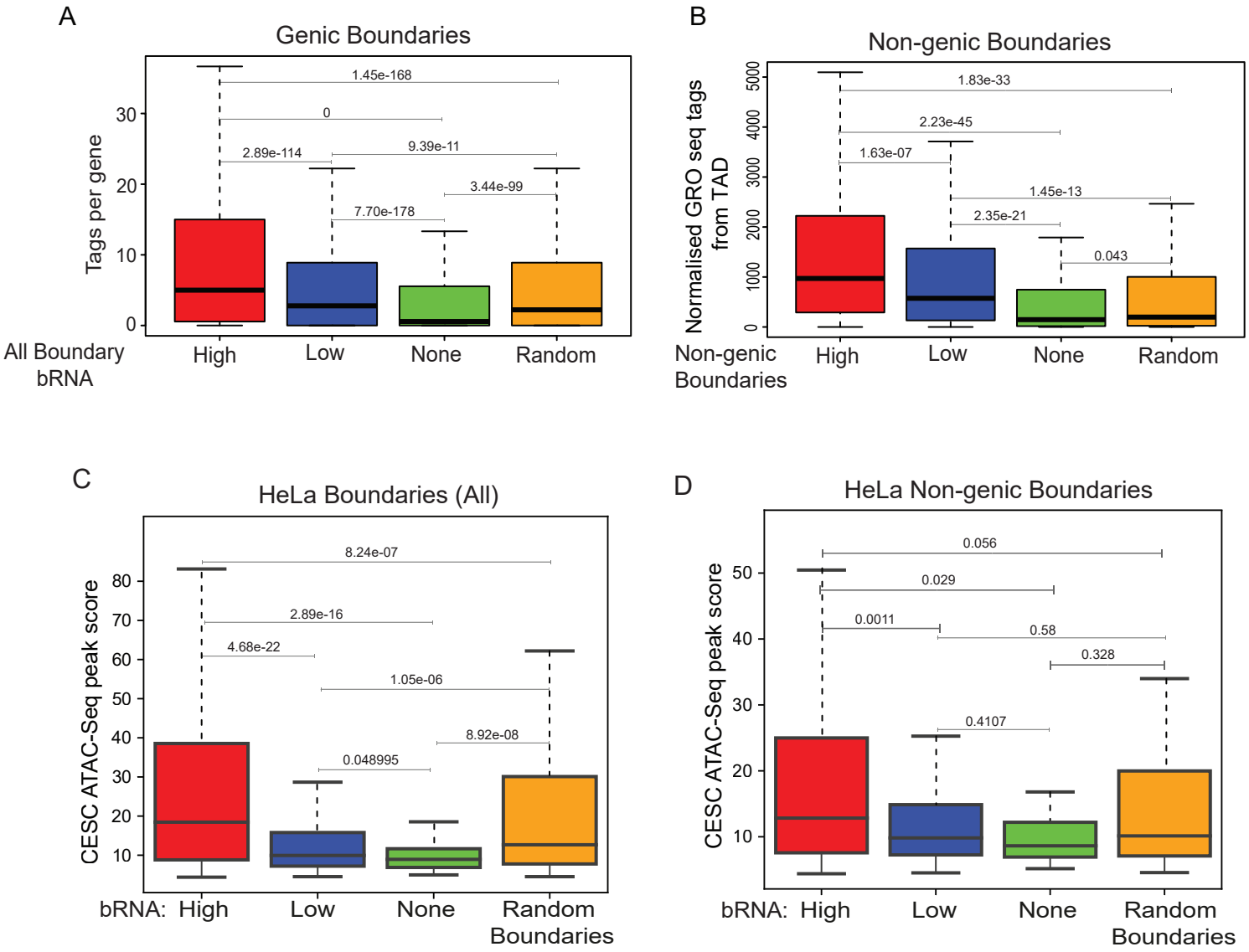

Islam and Saravanan et al. Supp Figure 7

Supp Figure 7. TAD transcription is correlated with transcribing boundaries: A. Box plots showing the normalized GRO-seq reads per gene within the TADs of high, low, non-transcribing and random boundaries. **B.** Box plots showing the normalized GRO-seq tags within the TADs of transcribing non-genic boundaries with high and low bRNAs, non-transcribing and random boundaries. **C.** Box plots showing the ATAC signal at All boundaries exhibiting different levels of bRNAs (From HeLa) vs. non-transcribing and random boundaries in Cervical Squamous Cell Carcinoma tumors from TCGA datasets. **D.** Box plots showing the ATAC signal at the non-genic boundaries exhibiting different levels of bRNAs (From HeLa) vs. non-transcribing and random boundaries in Cervical Squamous Cell Carcinoma tumors from TCGA datasets.

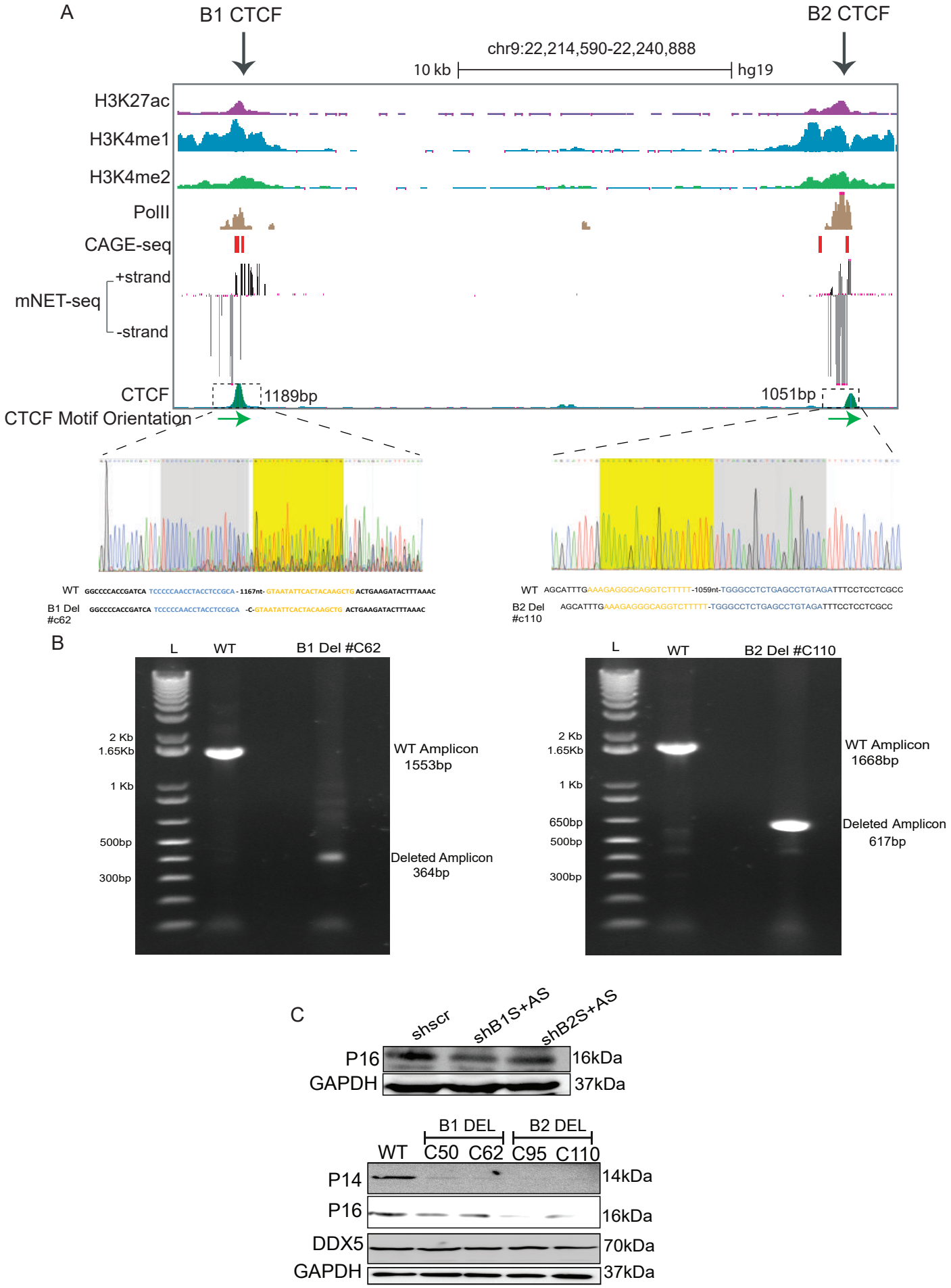

Islam and Saravanan et al Supp Fig. 8

Supp Figure 8. Deletion of B1 and B2 CTCF sites in INK4a/ARF TAD boundary: A. UCSC genome bowser track depicting the deleted B1 and B2 CTCF sites (boxed region at the bottom). The sites are overlaid with various histone marks, CAGE, NET-seq signal, CTCF peaks and CTCF orientation (Green arrows). The tracks zoom in to the chromatograms from sanger sequencing on deleted amplicon to verify the deletion. **B.** Agarose gel images showing the amplicons from surveyor assay from B1 and B2 deletions. **C.** Immunoblot showing the protein levels of p16 in Scr, shRNA against sense and anti-sense RNA at B1 and B2 CTCF sites (Upper panel). Immunoblot showing the protein levels of p14, p16, DDX5 and GAPDH in WT and, in cells with B1 and B2 CTCF sites deletions (Lower panel).

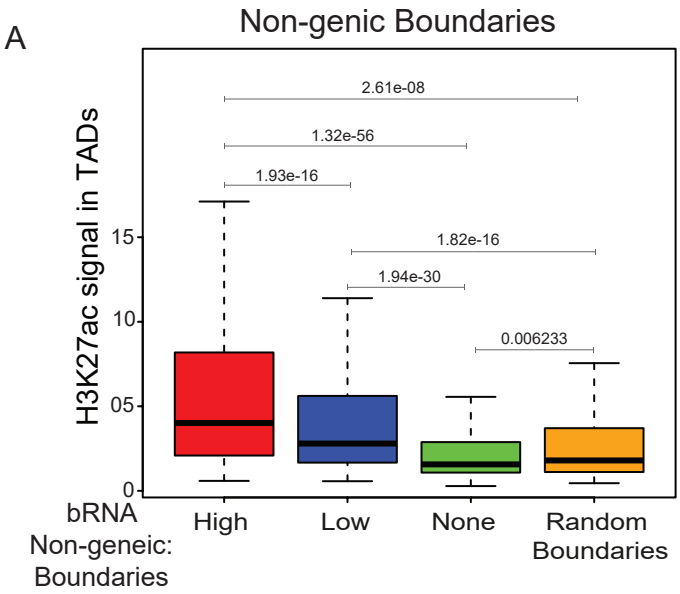

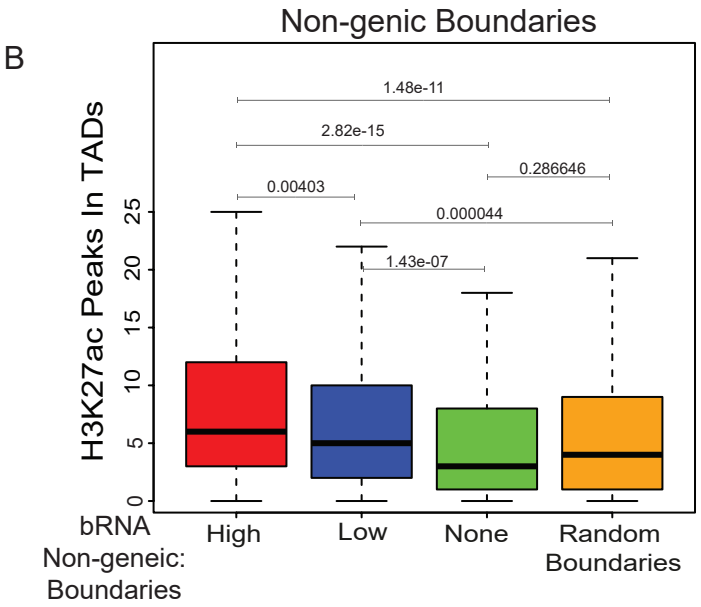

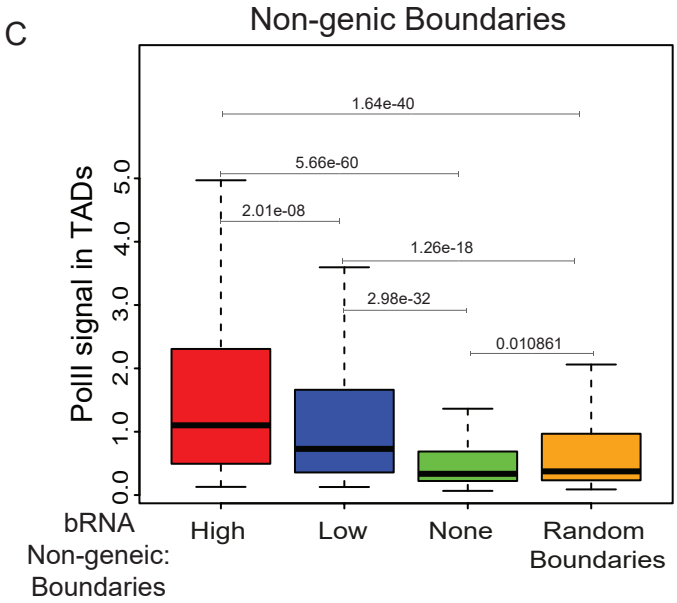

Islam and Saravanan Supp Fig. 9

Supp Figure 9. TADs with transcribing boundaries harbour more active enhancers: A. Boxplots displaying enrichment of H3K27ac in TADs with high, low transcribing non-genic HeLA boundaries vs. non-transcribing and random boundaries. **B.** Boxplot showing number of H3K27ac peaks within the TADs with non-genic transcribing boundaries with high and low bRNA vs. non-transcribing and random boundaries. **C.** Levels of PolII in TADs with different non-genic transcribing boundaries vs. non-transcribing and random boundaries.

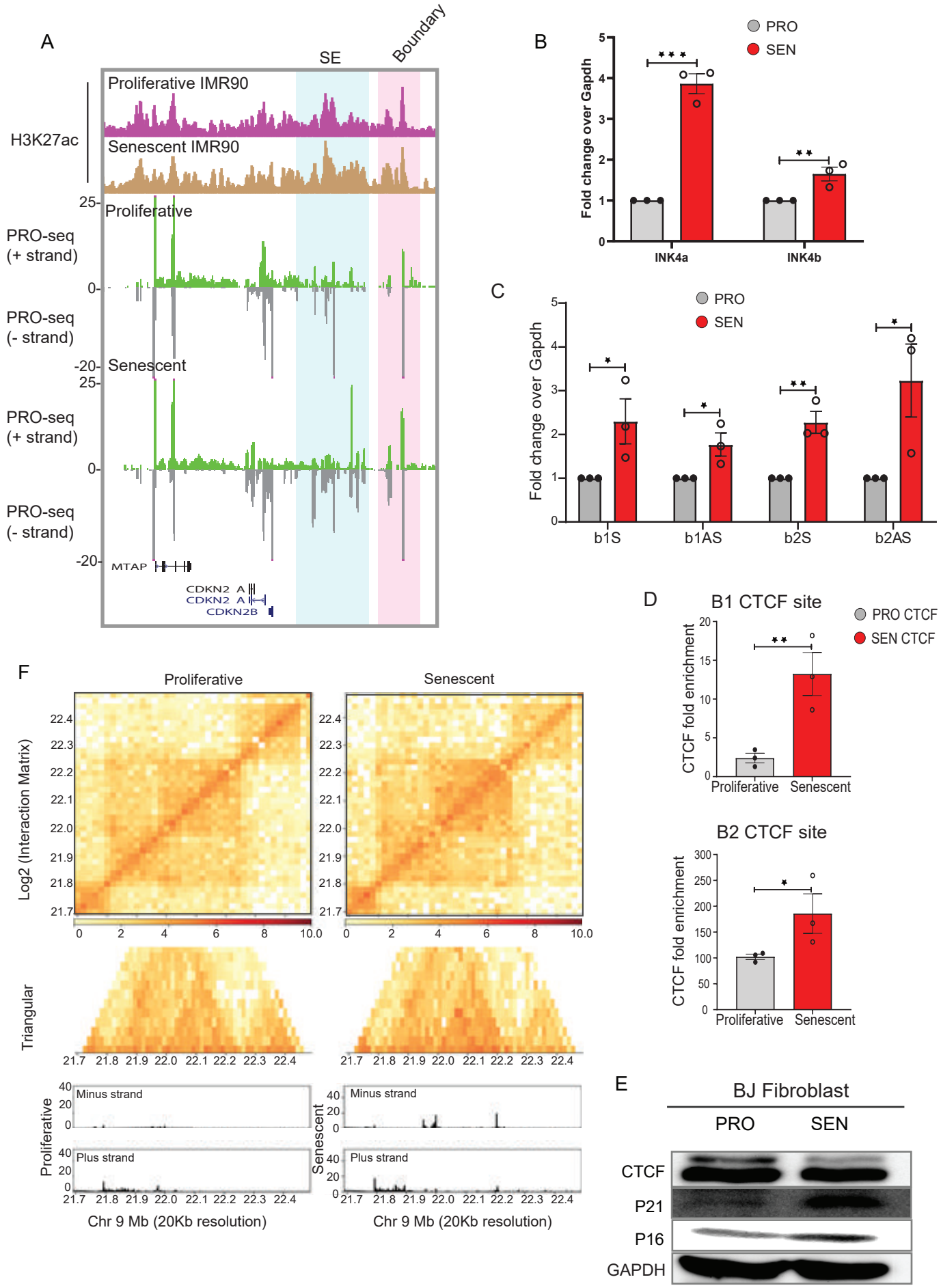

Islam and Saravanan et al. Supp Figure 10

Supp Figure 10. Transcriptional state of INK4a/ARF TAD in senescence : A. Browser images showing H3K27ac, PRO-seq reads on INK4A/ARF TAD from young and replicative senescent IMR90 fibroblasts. Highlighted regions depict super enhancer and boundary region. **B**. qRT-PCR plots show the fold change in expression of INK4a and INK4b in young and DNA damage induced senescent BJ fibroblasts. **C.** qRT-PCR plots show the fold change in expression of bRNA from B1 and B2 CTCF sites in young and DNA damage induced senescent BJ fibroblasts. **D.** ChIP qRT-PCRs showing the changes in fold enrichment of CTCF at B1 and B2 CTCF sites in young and DNA damage induced senescent BJ fibroblasts. Error bars denote SEM from three biological replicates. *p*-values were calculated by Student's two-tailed unpaired *t*-test in **B**, **C**, and **D .** $***p < 0.001, **p < 0.01, *p < 0.05, {}^{ns}p > 0.05$. **E.** Immunoblot showing the changes in protein levels of CTCF, p21, p16 and GAPDH in young and DNA damage induced senescent BJ fibroblasts. **F.** INK4a/ARF TAD structure in proliferating and senescent cells. Lower boxes represent the transcriptional levels.

Table 1: Oligonucleotide sequences used in the study

Primers used for ChIP-qPCRs

CTCF sites	Forward Primer (5'-3')	Reverse Primer (5'-3')
-T2	TAAATCTCCTGCCAGGAGG	GGCAGGTTCCATTTTACTTTGAG
-T1	GGCAGTACTGAGTTGACAC	CCCAGGAAACTGGACCTCTAA
B1	AGCTCTCTGCACCACATTGCCACTGCC	CCAACCTACCTCCGCAAGGACACC
B2	TTGAGGACATCTAGCGGCG	GCTGCAGATTCTGGAATGAGC
B3	GTCAGGACTAGGCCCATCTGAC	TAGGTGTCCAAGTGAAGATTAAAGAG
+T1	CAACTCCTTCCGAGTGGAAA	ACACTGTGACCGCTCCATTC
+T2	GCATAGATGTTTGGAGGGCAAC	TTACAGAATCTGGCTACTGCCC
INK4a	TCGCCAGGAGGAGGTCTGTGATTAC	CAGGTGGGTAGAGGGTCTGCAGC
ARF	ACCCAGGATATTCGGGACTCACTGAC	CGTCTCTAGCCCAGGCTAGGAGG
INK4b	CCGTCGTCCTTCTGCGGCTTG	AGTGAGGACTCCGCGACGCGT

Primers used for qRT-PCRs

mRNA/bRNA	Forward Primer (5'-3')	Reverse Primer (5'-3')
MTAP	TTGACAGGACCACTATGAGACCTC	AGGTCCCTCGATTGTGACCATT
INK4a	ATGGAGCCTTCGGCTGACT	CACCAGCGTGTCCAGGAAG
ARF	AACATGGTGCGCAGGTTCT	CACCAGCGTGTCCAGGAAG
INK4b	CGTTAAGTTTACGGCCAACG	CCATCATCATGACCTGGATCG
DDX5	CCTACCTTGTCCTTGATGAAGC	CACTCAGTTCAAGTGCACCA
CTCF	TACAAACACACCCACGAGAAG	GGGTAAACCGAGCATGACAA
b1S	CCACAGCAGAATAGAGCACC	AAGTCCAGCCAGTCTCAGCA
b1AS	TGAGGCTTGTAGGAACTCAAGTTC	AGTGGCAATGTGGTGCAGAG
b2S	ACAGAGGTCGGATGTTCGTG	TAAACCGCCGCTAGATGTCC
b2AS	CTCCTGAGCTCTAAGTGAGATAGAGG	GGTTATTCACTCACAGTGCTCTTCAG
sno RNA	CGTGTAGAGCACCGAAAACC	CACTCAGACCGCGTTCTCTC
pre c-MYC	CTTCTCTCCGTCCTCGGATTC	CCTTCCTAATAAGAGTGGCCCG
GAPDH	CGCTCTCTGCTCCTCCTGTT	CCATGGTGTCTGAGCGATGT

shRNAs used for knockdown

shRNA	Primer sequence (5'-3')
shRNA1 Boundary 1 S F	CCGGGAGTTGTGAGACCCTCATTTCCTCGAGGAAATGAGGGTCTCACAACTCTTTTTG
shRNA1 Boundary 1 S R	AATTCAAAAAGAGTTGTGAGACCCTCATTTCCTCGAGGAAATGAGGGTCTCACAACTC
shRNA2 Boundary 1 F	CCGGGGACCCTGAGCTGTGAATAACCTCGAGGTTATTCACAGCTCAGGGTCCTTTTTG
shRNA2 Boundary 1 R	AATTCAAAAAGGACCCTGAGCTGTGAATAACCTCGAGGTTATTCACAGCTCAGGGTCC
shRNA3 Boundary 1 S F	CCGGGAGTCCTAGCCAGGTAATATTCTCGAGAATATTACCTGGCTAGGACTCTTTTTG
shRNA3 Boundary 1 S R	AATTCAAAAAGAGTCCTAGCCAGGTAATATTCTCGAGAATATTACCTGGCTAGGACTC
shRNA1 Boundary 1 AS	CCGGCTGGCTCCGGCTGGTTTAAATCTCGAGATTTAAACCAGCCGGAGCCAGTTTTTG

F	
shRNA1 Boundary 1 AS R	AATTCAAAAACTGGCTCCGGCTGGTTTAAATCTCGAGATTTAAACCAGCCGGAGCCAG
shRNA2 Boundary 1 AS F	CCGGCGGCTCTGCTTTCAGCTATAACTCGAGTTATAGCTGAAAGCAGAGCCGTTTTTG
shRNA2 Boundary 1 AS R	AATTCAAAAACGGCTCTGCTTTCAGCTATAACTCGAGTTATAGCTGAAAGCAGAGCCG
shRNA3 Boundary 1 AS F	CCGGAGGTAAGATGTAAGCATTAATCTCGAGATTAATGCTTACATCTTACCTTTTTTG
shRNA3 Boundary 1 AS R	AATTCAAAAAAGGTAAGATGTAAGCATTAATCTCGAGATTAATGCTTACATCTTACCT
shRNA1 Boundary 2 S F	CCGGCGCAATCCAACTATTCAATTTCTCGAGAAATTGAATAGTTGGATTGCGTTTTTG
shRNA1 Boundary 2 S R	AATTCAAAAACGCAATCCAACTATTCAATTTCTCGAGAAATTGAATAGTTGGATTGCG
shRNA2 Boundary 2 S F	CCGGGCTTTCCTGAAGGAGAGTAATCTCGAGATTACTCTCCTTCAGGAAAGCTTTTTG
shRNA2 Boundary 2 S R	AATTCAAAAAGCTTTCCTGAAGGAGAGTAATCTCGAGATTACTCTCCTTCAGGAAAGC
shRNA3 Boundary 2 S F	CCGGTAGCAATGGCAGAACCTATTTCTCGAGAAATAGGTTCTGCCATTGCTATTTTTG
shRNA3 Boundary 2 S R	AATTCAAAAATAGCAATGGCAGAACCTATTTCTCGAGAAATAGGTTCTGCCATTGCTA
shRNA1 Boundary 2 AS F	CCGGAGGAACTACATTGACTTATTTCTCGAGAAATAAGTCAATGTAGTTCCTTTTTTG
shRNA1 Boundary 2 AS R	AATTCAAAAAAGGAACTACATTGACTTATTTCTCGAGAAATAAGTCAATGTAGTTCCT
shRNA2 Boundary 2 AS F	CCGGCGACCTCTGTAAATGAAATAGCTCGAGCTATTTCATTTACAGAGGTCGTTTTTG
shRNA2 Boundary 2 AS R	AATTCAAAAACGACCTCTGTAAATGAAATAGCTCGAGCTATTTCATTTACAGAGGTCG
shRNA3 Boundary 2 AS F	CCGGTGGATTGCGATTTCCTGAAATCTCGAGATTTCAGGAAATCGCAATCCATTTTTG
shRNA3 Boundary 2 AS R	AATTCAAAAATGGATTGCGATTTCCTGAAATCTCGAGATTTCAGGAAATCGCAATCCA

Primers used for RNA IP

Target	**Primer sequence (5'-3')**
B1 S in pCDNA 3 Box B F	AGACTGGCGGCCGCTAGGCCTCAAGGACTGCAA
B1 S in pCDNA 3 Box B R	AGACTGTCTAGACTCCTGGGAGCCAGAGAA
B1 AS in pCDNA 3 Box B F	AGACTGGAATTCAGTAGGTCGCATGCAACCACA
B1 AS in pCDNA 3 Box B R	AGACTGGCGGCCGCTCCTACATCAGCTGTGGCACA
B2 S in pCDNA 3 Box B F	AGACTGGAATTCGCCTCTGAGCCTGTAGAGACCAA
B2 S in pCDNA 3 Box B R	AGACTGGCGGCCGCCTCTGGGTGAGGCAGTGAACAC
B2 AS in pCDNA 3 Box B F	AGACTGGAATTCATCCTCCAGGACCACAGCAGT
B2 AS in pCDNA 3 Box B R	AGACTGGCGGCCGCGCATACCCTGGAGTGAGAGGTTG
E8 in pCDNA 3 Box B F	AGACTGGAATTCAATGCCATATGGTGGCAATG
E8 in pCDNA 3 Box B R	AGACTGGCGGCCGCATCTGTTCCTTGCCTCTTCCAC

gRNAs used for deletions and CRISPRi

gRNA	Sequence
B1 DEL gRNA 1	TTAAATTGGTGTCCTTGCGG
B1 DEL gRNA 2	GTAGTGAATATTACCTGGCT
B2 DEL gRNA 1	CAGACTTCCGTAGTCCCCAT
B2 DEL gRNA 2	TTGGGTAGCATCTTCATCGG
MTAP gRNA 1	AGCAGTGCGGAGACCAGGGG
MTAP gRNA 2	CTCACTTGCCGCGCGAGGAG
INK4a gRNA 1	AGCCGTTTTACACGCAGGAG
INK4a gRNA 2	GACAGGACAGTATTTGAAGC
ARF gRNA 1	ATGCGCCCCGGACTTTTCGA
ARF gRNA 2	CTGCCCCCTTAACTGCAGAC
INK4b gRNA 1	AAAGAATTCCGTTTTCAGCT
INK4b gRNA 2	CTAGGAAGGAGAGAGTGCGC

Surveyor Oligos

Target	Forward Primer (5'-3')	Reverse Primer (5'-3')
B1 DEL	TGGAGTGGTAGTAGTGTGGGAAG	GTACGAGGGTTCTCTTTTGCTTG
B2 DEL	CACAACCCCCATCTCTCTGTAAC	TGAAGTGAGGGGAGTAGACAAGG

4C oligos for enhancer and Promoter viewpoints

View Point	Primer sequence (5'-3')
Enhancer F	AATGATACGGCGACCACCGAACACTCTTTCCCTACACGACGCTCTTCCGATCTGGTATTCTGACTAGAAGCTT
Enhancer R	CAAGCAGAAGACGGCATACGATAGTGGTGCTACAGTACCAC
Promoter F	AATGATACGGCGACCACCGAACACTCTTTCCCTACACGACGCTCTTCCGATCTGGAGGAGCTAGGGCAAGCTT
Promoter R	CAAGCAGAAGACGGCATACGACAGATGGATAAGTAGTAGCAAG

Table 3: Datasets used in the study

Experiment	Annotation	Accession Number	References
HeLa GRO-seq	SRR1596500	GSM1518913	Andersson et al., 2014. Nat Commun.
HeLa GRO-seq	SRR1596501	GSM1518914	Andersson et al., 2014. Nat Commun.
HeLa HiC	SRR1050968	-	Burton et al., 2013. *Nat Biotechnol*.
HeLa HiC	SRR1050969	-	Burton et al., 2013. *Nat Biotechnol*.
HeLa HiC	SRR3203899-SRR3203906	-	Rao et al., 2014. Cell.
HeLa PolII	wgEncodeSydhTfbsHelas3Pol2StdSig	GSM935395	ENCODE
HeLa CTCF	wgEncodeUwTfbsHelas3CtcfStdRawRep1	GSM749729	ENCODE
HeLa CTCF	wgEncodeUwTfbsHelas3CtcfStdRawRep2	GSM749739	ENCODE
HeLa H3K27ac	wgEncodeBroadHistoneHelas3H3k27acStdSig	GSM733684	ENCODE
IMR90 HiC	SRR5494761	GSM2595584	Zirkel etal., 2018. Mol Cell
IMR90 PRO seq	SRR6205688	GSM2828779	Sen et al., 2019. Mol Cell
IMR90 CTCF	wgEncodeSydhTfbsImr90CtcfbIggrabSig	GSM935404	ENCODE
K562 HiC	SRR1658693-SRR1658702	GSM1551618-GSM1551623	Rao et al., 2014. Cell.
K562 CTCF	wgEncodeUwTfbsGm12878CtcfStdAlnRep1	GSM749690	ENCODE
K562 GROseq	SRR1552484	GSM1480325	Core et al., 2014. Nat Genet.
HeLa_GRO-Seq	SRR5109939	GSM2428725	Bouvy-Liivrand et al., 2017. Nucleic Acids Res
PRO-Seq-DMSO	SRR5799635	GSM2692352	Nilson et al., 2017.Nucleic Acids Res
Total mNET-Seq	SRR4436479	GSM2357382	Schlackow et al., 2017. Mol Cell